

Multiport Analytical Pixel Electromagnetic Simulator (MAPES) for AI-assisted RFIC and Microwave Circuit Design

Junhui Rao, *Member, IEEE*, Yi Liu, *Member, IEEE*, Jichen Zhang, *Student Member, IEEE*, Zhaoyang Ming, *Student Member, IEEE*, Tianrui Qiao, *Member, IEEE*, Yujie Zhang, *Member, IEEE*, Chi Yuk Chiu, *Senior Member, IEEE*, Hua Wang, *Fellow, IEEE*, and Ross Murch, *Fellow, IEEE*

Abstract—This paper proposes a novel analytical framework, termed the Multiport Analytical Pixel Electromagnetic Simulator (MAPES). MAPES enables efficient and accurate prediction of the electromagnetic (EM) performance of arbitrary pixel-based microwave (MW) and RFIC structures. Inspired by the Integrated Internal Multiport Method (IMPM), MAPES extends the concept to the pixel presence/absence domain used in AI-assisted EM design. By introducing virtual pixels and diagonal virtual pixels and inserting virtual ports at critical positions, MAPES captures all horizontal, vertical, and diagonal electromagnetic couplings within a single multiport impedance matrix. Only a small set of full-wave simulations (typically about 1% of the datasets required by AI-assisted EM simulators) is needed to construct this matrix. Subsequently, any arbitrary pixel configuration can be evaluated analytically using a closed-form multiport relation without additional full-wave calculations. The proposed approach eliminates data-driven overfitting and ensures accurate results across all design variations. Comprehensive examples for single- and double-layer CMOS processes (180 nm and 65 nm) and PCBs confirm that MAPES achieves high prediction accuracy with 600-2000 \times speed improvement compared to CST simulations. Owing to its efficiency, scalability and reliability, MAPES provides a practical and versatile tool for AI-assisted MW circuit and RFIC design across diverse fabrication technologies.

Index Terms—Artificial intelligence; design automation; electromagnetic coupling; electromagnetic simulation; machine learning; microwave circuits; multiport analytical modeling; pixel-based design; RFIC design.

I. INTRODUCTION

As the deployment of 5G progresses and extensive research into future 6G wireless networks continues, the development of various new wireless devices is anticipated, each with specific requirements and specifications for RF

This work was supported by Hong Kong Research Grants Council Area of Excellence Grant AoE/E 601/22-R. (Corresponding author: Junhui Rao.)

Junhui Rao, Yi Liu, Jichen Zhang, Zhaoyang Ming, Tianrui Qiao and Chi Yuk Chiu are with the Department of Electronic and Computer Engineering, the Hong Kong University of Science and Technology, Hong Kong (e-mail: jraoaa@connect.ust.hk).

Yujie Zhang is with School of Electrical and Electronic Engineering, Nanyang Technological University (NTU), Singapore (e-mail: yujie.zhang@ntu.edu.sg).

Hua Wang is with the School of Information Technology and Electrical Engineering, ETH Zürich, 8092 Zürich, Switzerland (e-mail: wanghua@ethz.ch).

R. Murch is with the Department of Electronic and Computer Engineering and Institute for Advanced Study (IAS) at the Hong Kong University of Science and Technology, Hong Kong (e-mail: eermurch@ust.hk).

modules [1], [2], [3], [4]. The traditional design and development of a large variety of microwave (MW) circuits and radio frequency integrated circuits (RFICs), particularly electromagnetic (EM) structures such as matching networks, combiners, splitters, quadrature hybrids, and couplers, have heavily relied on human experience and prior knowledge. This reliance necessitates significant human and computational resources for design iterations. Additionally, these designs have historically explored only a limited design space defined by a narrow set of tunable parameters [5], [6], [7], [8], [9], such as the width and length of transmission lines in matching networks, which restrict the searchable design space and limits achievable circuit performance.

To address these challenges, recent studies have extensively explored the use of artificial intelligence (AI) methods to automate the design and synthesis of EM structures for MW circuits and RFICs [10], [11], [12], [5], [13]. In order to fully explore all possibilities within the design area, the entire design space is often divided into arrays of tiny pixels. For instance, in [5], a chip measuring 300 \times 300 μm is discretized into 16 \times 16 pixels. It is also noteworthy that the electrical sizes of pixels in those AI-designed RFICs can be very small (\sim 1/100 λ level) enabled by the high resolution of integrated circuit processes. This enables AI techniques to fully explore the design space for RFICs. By configuring the presence or absence of each pixel, various EM structures can be explored to cover the entire possible design space. The process of using AI for rapid design and synthesis of EM structures can be summarized in two main parts.

Firstly, given the significantly large number of possibilities (such as $2^{256} \approx 10^{77}$ possible structures for the 16 \times 16 pixel configuration), full-wave simulations become unsuitable due to the unaffordable computational load. Consequently, the development of highly efficient EM simulators to predict the performance of arbitrary EM structures (such as scattering parameters) becomes necessary. By training on a large dataset obtained through full simulations, convolutional neural network (CNN)-based EM simulators [11], [10] and deep CNN-based EM simulators have been proposed [5], [14], [13], demonstrating decent accuracy in predictions.

Secondly, for specific specifications (targeted scattering parameters), the developed efficient EM simulators can be utilized for inverse synthesis of EM structures using heuristic algorithms [5], [15], such as genetic algorithms (GA), simu-

lated annealing, or generative AI tools such as auto-encoders, tandem neural networks [16], or diffusion models [12].

While the aforementioned AI-assisted techniques can significantly enhance the efficiency of designing MW circuits or RFICs to within minutes, several challenges remain:

- 1) *Generation of Training Datasets*: Due to the vast number of possible configurations, ensuring high accuracy for simulators necessitates the simulation of a large volume of training data using traditional full-wave simulations, such as CST or HFSS. For instance, generating a training dataset of 180,000 samples for a single-layer 25×25 pixel configuration requires approximately 13 days on a high-performance computer with 400 CPU cores [14]. This duration increases significantly when multi-layer structures and inter-layer vias are considered.
- 2) *Selection of Training Datasets*: Despite simulating a relatively large volume of training data, these datasets represent only a tiny fraction of the total possible EM structures. For example, the 180,000 training samples account for merely $1.29 \times 10^{-183}\%$ of the total design space [14]. Thus, the training dataset must be meticulously selected to prevent potential bias and overfitting issues. These occur in the AI-assisted simulator [17], [18] when the simulator exhibits high accuracy on validation/test datasets but poor accuracy on inputs significantly different from the training data. In other words, given the exceedingly small size of the training data relative to the entire design space, the ability of the trained EM simulators to generalize across all design spaces is uncertain.
- 3) *Storage and Handling of Training Datasets*: The substantial storage requirements and hardware demands for managing large datasets pose significant challenges. For instance, the aforementioned 180,000 training dataset would require approximately 180 GB of storage if each data file is 1 MB. These requirements grow considerably with the expansion of the design space and the inclusion of multi-layer structures. This limitation is one of the factors restricting the increase in training dataset size, which is necessary for developing more accurate EM simulators.

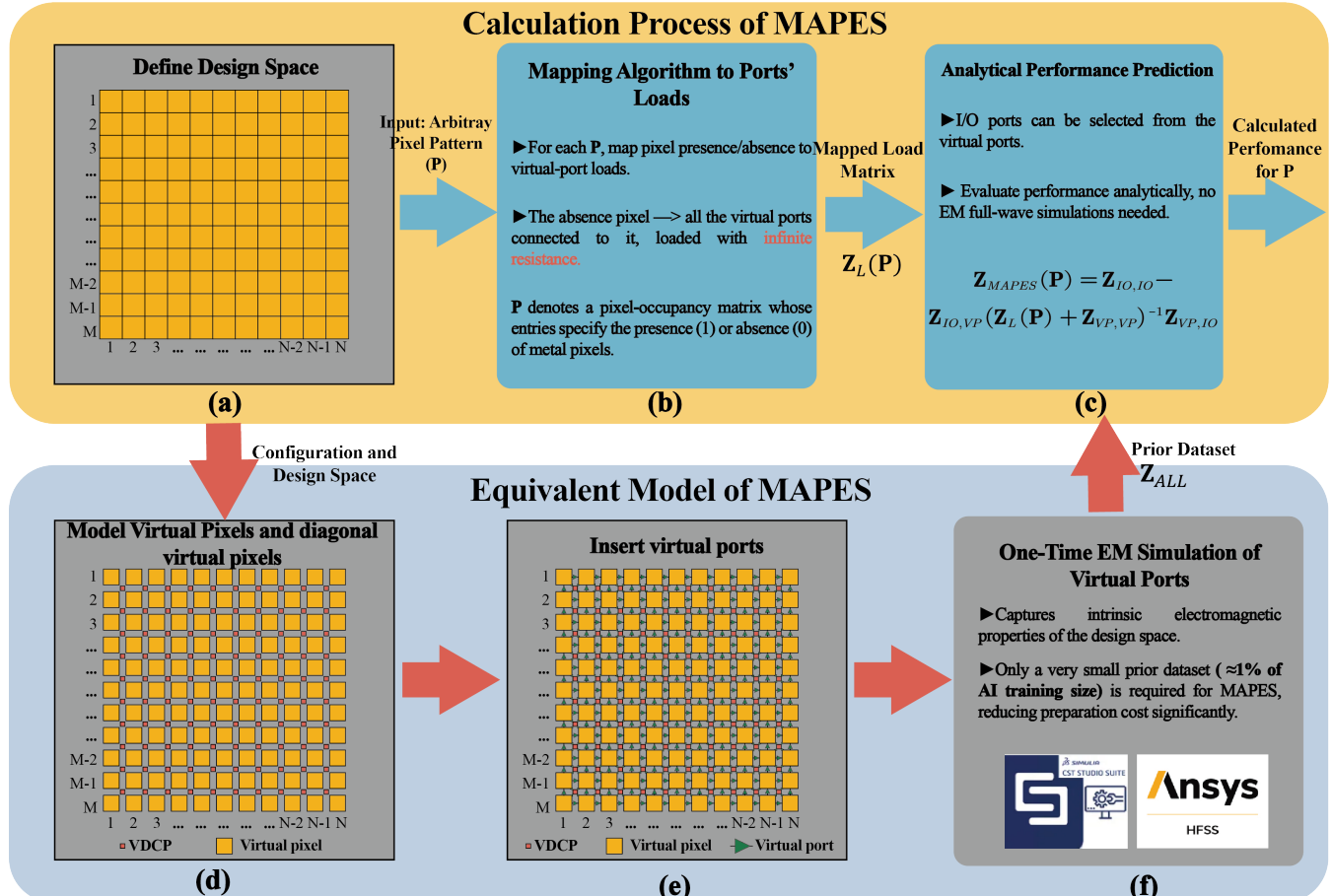
On the other hand, there is another related area: pixel antenna design [19], [20], [21], [22], [23], [24], [25], [26], where the structures of antennas are discretized into an array of pixels. Unlike the optimization approach focusing on the presence or absence of pixels, these studies emphasize optimizing the interconnections between pixels, with gaps existing between adjacent pixels. To facilitate efficient optimization, methods such as the Integrated Internal Multiport Method (IMPM) [20] are employed to calculate the performance of antennas or MW structures. Consequently, unlike AI-assisted MW circuit and RFIC research [10], [11], [12], [5], [13], where the input is the presence or absence of pixels, the input for IMPM is the connection states between pixels.

IMPM has demonstrated a powerful ability to efficiently calculate the performance of pixel arrays with arbitrary connection configurations among these pixels [20]. However, it

cannot be directly applied to calculate the performance of arbitrary presence/absence configurations of pixels in RFICs due to several limitations. Firstly, the input of IMPM (connection configurations) does not adequately reflect the presence or absence of pixels. Additionally, IMPM does not effectively represent the states of diagonally connected pixels in RFICs. Although efforts have been made to include diagonal connections in pixel antennas [27], this approach is unsuitable for RFICs due to the extra layer and vias required for overlapping diagonal connections. Furthermore, the input/output (I/O) positions of pixel antennas are typically fixed, whereas in AI-assisted RFIC and MW circuit design, I/O ports are preferred to be in arbitrary positions and numbers across the design space to fully explore the design possibilities.

In this paper, we address the challenges associated with AI-based EM simulators by proposing a Multiport Analytical Pixel Electromagnetic Simulator (MAPES), inspired by IMPM. We conduct a comprehensive investigation into its methodology, provide examples, and verify its performance experimentally. MAPES employs multiport system theory to accurately and efficiently calculate the performance of arbitrary EM structures. It simulates EM performance using a single analytical formula by incorporating all design space characteristics into a Z matrix. The main contributions of MAPES in this paper are summarized as follows:

- 1) *Extension of IMPM to AI-assisted MW Circuit/RFIC*: To bridge the gap between IMPM and pixel presence/absence patterns in AI-assisted RFIC design, MAPES introduces diagonal virtual pixels inserted at the corners of all pixels to enable diagonal connections. Virtual ports are also inserted between adjacent pixels and diagonal virtual pixels. These virtual ports ensure that all RF characteristics of the design space are fully captured in the Z matrix for them. Consequently, arbitrary shapes formed by pixels can be converted into corresponding connection state configurations, leading to a load matrix connected to the Z matrix. The performance of these structures can then be analytically and efficiently calculated using multiport network theory.
- 2) *Small Prior Dataset Required*: AI-assisted EM simulators require large training datasets, presenting challenges in data generation and limiting scalability to larger design spaces. In contrast, MAPES requires only a prior dataset comprising the Z matrix of virtual ports, obtained through a significantly smaller number of full-wave simulations. This prior dataset is typically only about 2~5% the size of the training dataset for AI-assisted EM simulators. For instance, for a single-layer 25×25 pixel configuration, only 3.5K prior datasets are needed compared to 180K training datasets [14].
- 3) *Generalization to All Possible Structures*: AI-assisted EM simulators often face challenges such as overfitting and biases due to the limited coverage of the training dataset [14], [17], [18]. In contrast, MAPES, even with a smaller prior dataset, avoids these issues. Each simulation in the prior dataset contains comprehensive physical information between the simulated port and



Note: In (d)–(e), diagonal virtual pixels with four associated virtual ports are used as a conservative way to model diagonal connections between pixels in original design space. This choice is compatible with different meshes and solvers (e.g., CST, HFSS), but for some solvers it may be sufficient to use only two diagonal ports per pixel corner, provided the accuracy is verified. All subsequent MAPES steps remain unchanged.

Fig. 1: Overview of the MAPES methodology detailing the calculation process (top row) and the equivalent model of MAPES (bottom row). (a) The pixel-based design space is defined by the pixel occupancy matrix \mathbf{P} whose binary entries model the presence (1) or absence (0) of pixels; (b) map the design space \mathbf{P} to the virtual port load matrix using the proposed mapping algorithm; (c) analytically predict performance at the chosen I/O ports via the closed-form multiport method; (d) the equivalent model of the design space \mathbf{P} is created using virtual pixels and inserting diagonal virtual pixels at pixel corners; (e) insert virtual ports between adjacent virtual pixels and diagonal virtual pixels; (f) perform full-wave simulations (e.g., CST, HFSS) to extract the impedance matrix capturing all key electromagnetic effects of the equivalent model.

all other ports. The predicted results of MAPES are calculated using formulas rigorously derived from the \mathbf{Z} matrix based on microwave theory, ensuring accurate predictions for arbitrary pixel patterns and I/O ports.

- 4) *Applicability to Various Fabrication Processes:* The smaller size of the prior dataset required by MAPES, coupled with lower computational demands, allows it to extend to larger design spaces with more pixels or multi-layer structures. Thus, MAPES is a versatile simulator applicable to various fabrication processes, from PCBs with multiple layers to RFICs with different processes and metal layers.
- 5) *Verification of MAPES:* To demonstrate the efficacy of MAPES, we include comprehensive examples ranging from single-layer CMOS 180nm to double-layer CMOS 65nm processes, and from single-layer PCBs to double-

layer PCBs. The results show good accuracy compared to full-wave simulations, with MAPES achieving a 600–2000 \times speedup. Notably, the design space includes metal vias between layers in both PCB and CMOS 65nm examples, which were not considered in previous AI-assisted EM simulator research [5], [10], [11], [12], [13].

Another technique conceptually related to MAPES, the Method of Moments (MoM)-based "efficient calculator" in [28], precomputes the impedance matrix of a "mother" structure and accelerates exploration by directly manipulating this matrix (removing rows/columns) to evaluate substructures, thereby avoiding repeated matrix refills/factorizations. However, that framework was devised for planar plates and thin-wire geometries excited by voltage/current sources, making it difficult to incorporate vertical ports, vias, and lumped or active components-elements that are intrinsic to MW/RFIC

pixels. In contrast, MAPES natively captures horizontal and vertical couplings and supports arbitrary loads, including realistic nonzero via impedances and comprehensive I/O modeling. Furthermore, the MAPES prior-data impedance matrix can be obtained directly from commercial tools (e.g., CST, HFSS), while the mesh-level MoM impedance matrix is typically inaccessible without custom implementations. Thus, while both methods reuse a precomputed impedance representation, MAPES delivers broader modeling flexibility, easier tool integration, and superior scalability for large pixel design spaces. Finally, MoM requires fine meshing (e.g., RWG basis on triangular elements [29]) to resolve pixel details, inflating the number of unknowns and yielding dense matrices that scale poorly, especially for multilayer arrays, whereas MAPES places ports only at electrically essential locations, producing a far more compact representation and smaller matrices. It is worth noting that the recently proposed precomputed numerical Green-function framework [30] likewise absorbs the static environment into a single operator obtained from full-wave solvers, but it operates on voxel- or mesh-level field unknowns, so its system matrices remain substantially larger than those of MAPES and scale with mesh density, similar to the MoM-based efficient calculator.

The remainder of this paper is organized as follows. Section II details the MAPES methodology, including the construction of virtual pixels and diagonal virtual pixels, insertion of virtual ports, extraction of the prior impedance matrix from full-wave simulations, the pixel-to-load mapping algorithm, and the closed-form multiport formulation used for analytical prediction. Section III presents four case studies that validate MAPES across technologies and scales: a CMOS 180 nm single-layer layout, a CMOS 65 nm double-layer layout with vias, a single-layer PCB, and a double-layer PCB with vias with S-parameter comparisons against CST. Section IV provides a comprehensive comparison and discussion, quantifying accuracy and speed versus full-wave solvers, contrasting MAPES with AI-assisted EM simulators, clarifying modeling assumptions and one-time pre-simulation settings, outlining potential applications (as a simulator, dataset generator, and physics-informed backbone), and discussing connections and differences with MoM-based efficient calculators. Section V concludes the paper.

II. METHODOLOGY OF MAPES

The core concept of MAPES is illustrated in Fig. 1 where the calculation process and the equivalent model are shown. Starting from the original physical pixel design space in Fig. 1(a), we construct an equivalent model based on a modified virtual pixel structure, as shown in Fig. 1(d). Virtual ports are inserted between the virtual pixels (Fig. 1(e)) and these virtual ports can be loaded with connections to form any equivalent structure in the design space (Fig. 1(a)). This virtual model is analyzed using efficient techniques (described later) to accurately predict the performance of the original design space, as illustrated in Fig. 1(c). The construction and use of this equivalent model proceeds through several well-defined steps.

We first create an array of virtual pixels and insert diagonal virtual pixels at the pixel corners, as in Fig. 1(d). Virtual ports are then introduced to capture all relevant horizontal, vertical, diagonal, and (optionally) inter-layer interactions across the design space (Fig. 1(e)). A single round of full-wave simulations for these virtual ports yields the impedance matrix \mathbf{Z}_{ALL} , which embeds the intrinsic EM couplings of the entire design space. This matrix is computed only once, greatly reducing the overall computational burden of MAPES. We denote the "design space", \mathbf{P} , as a pixel-occupancy matrix whose entries specify the presence (1) or absence (0) of metal pixels (or vias) at each location in the discretized MW/RFIC layout domain in Fig. 1(a). For any physical pixel configuration in the original design space (Fig. 1(a)), a straightforward mapping algorithm converts the presence/absence pattern (\mathbf{P}) into a load matrix on the non-I/O virtual ports (Fig. 1(b)). Using a closed-form multiport method, MAPES then computes the I/O response $\mathbf{Z}_{\text{MAPES}}(\mathbf{P})$ directly from \mathbf{Z}_{ALL} and the mapped loads, without any additional full-wave simulations. This enables fast and accurate performance prediction and efficient exploration of large MW/RFIC pixel design spaces.

The details of these steps are presented in Subsection II A to D. Throughout this paper, the terms "pixel" and "pixel array" refer to the pixels in the original design space, in which pixels are placed contiguously without gaps. In contrast, "virtual pixel" and "diagonal virtual pixel" denote the elements of the equivalent model used in MAPES.

A. Virtual Pixel Configurations for MAPES

To characterize the physical properties across the entire design space, a comprehensive equivalent model needs to be developed. In this work we utilize an efficient approach based on virtual pixels and virtual ports. Because the original design space is formed by an array of seamlessly placed pixels, direct insertion of virtual ports is not feasible. Therefore, we first construct an alternative virtual pixel array over the same design area and augment it with diagonal virtual pixels, as shown in Fig. 1(d).

First, the original pixels are mapped to virtual pixels in a one-to-one manner, maintaining their central locations while slightly reducing their physical dimensions to allow for the insertion of virtual ports between them. However, this configuration alone does not fully capture the relationships between diagonally connected pixels. To address this, we introduce an array of diagonal virtual pixels located at the corners of the virtual pixels. These diagonal virtual pixels are smaller than the gaps between the virtual pixels, as shown in the detailed view of Fig. 2.

It should be noted that the use of diagonal virtual pixels with four virtual ports connected to each of them (as introduced in the following subsection), is a conservative modeling choice intended to accurately capture diagonal connections between pixels in the original design space. This construction is compatible with various mesh settings (e.g., hexahedral and tetrahedral meshes) and full-wave solvers (e.g., the CST transient solver and the HFSS frequency-domain solver). For some solvers, however, using diagonal virtual pixels may

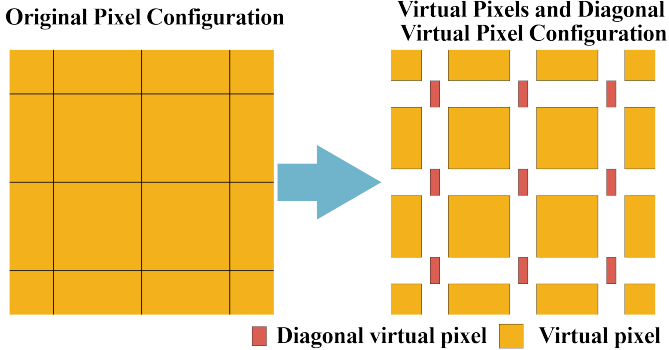


Fig. 2: Magnified view of the design space (left) and the equivalent model (right). The model (right) consists of virtual pixels and diagonal virtual pixels in MAPES.

be unnecessary, and the scheme can be simplified to using only two diagonal ports at each pixel corner, provided that the resulting accuracy is verified. Regardless of the specific representation of diagonal connections, the remaining steps and procedures of MAPES are identical to those described in this paper.

B. Virtual Ports and Impedance Matrix

With the virtual pixels and diagonal virtual pixels modeled over the design space, virtual ports are inserted as shown in Fig. 1(e) and in the detailed view of Fig. 3.

The insertion of virtual ports is organized into three sets. The first set comprises virtual ports placed between adjacent virtual pixels to capture physical properties in the vertical and horizontal directions of original pixels. The second set contains virtual ports between diagonal virtual pixels and adjacent virtual pixels to characterize diagonal interactions of original pixels. The final set consists of virtual ports between virtual pixels and the ground. These ports facilitate the definition of I/O ports by capturing the coupling between pixels and ground. Typically, these ground ports are placed between all outer virtual pixels and the ground to allow flexible I/O placement.

For multi-layer configurations, an optional additional set of virtual ports can be introduced. Extra virtual ports can be inserted between corresponding virtual pixels on adjacent layers to capture the electromagnetic properties of potential vias between layers, thereby extending the design space to include inter-layer connections that were not considered in previous works [5], [10], [11], [12], [13].

For a design space with L layers of $M \times N$ (row \times column) pixels, without considering virtual ports between different layers, the total number of virtual ports, Q , is given by:

$$Q = L(6MN - 3M - 3N + 4), \quad (1)$$

while including the virtual ports between different layers for vias, the total number of virtual ports Q is:

$$Q = L(6MN - 3M - 3N + 4) + (L - 1)MN. \quad (2)$$

With the inserted virtual ports, the RF properties across the entire design space can be comprehensively captured,

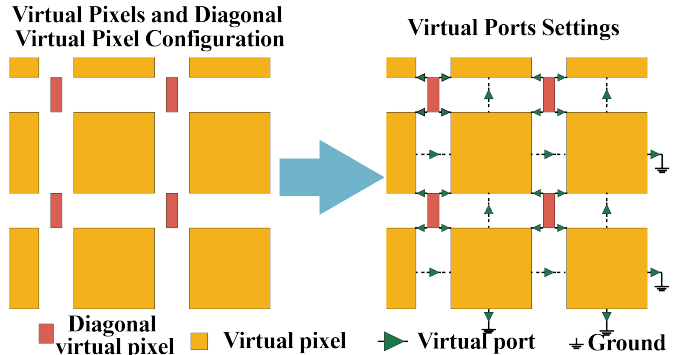


Fig. 3: Magnified view of the virtual pixel structure (left) and the insertion of virtual ports (right), including horizontal, vertical and diagonal virtual ports in the MAPS methodology.

as shown in Fig. 1 (f). Full-wave simulations can then be performed to obtain the impedance matrix, $\mathbf{Z}_{\text{ALL}} \in \mathbb{C}^{Q \times Q}$, which includes all necessary information for calculating the performance of arbitrary input pixel patterns. It is worth noting that other equivalent matrices, such as the S-parameter matrix or conductance matrix, can also be used in MAPES if needed.

This impedance matrix, \mathbf{Z}_{ALL} , constitutes the entire prior dataset required by MAPES. Obtaining it requires Q full-wave simulations using CST, HFSS, or other simulation software. The computational load is significantly reduced compared to the training data generation required by prior AI-assisted techniques, with full-wave simulation time or computational load being only about 1% of that required by AI-assisted EM simulators.

However, for designs involving radiation performance, the impedance matrix (or equivalents) alone may not suffice. Additional data, such as the radiation patterns of each virtual port, should also be obtained. Nevertheless, acquiring radiation properties does not significantly increase the computational load when preparing the prior data, as both Z-parameters and radiation patterns can be obtained simultaneously in a single full-wave simulation for each port. In this paper, MAPES is primarily focused on the design of MW circuits and RFICs, which typically only need Z-parameters (or equivalent S-parameters) performance without involving radiation properties, so we consider only impedance (scattering parameters) performance in this paper.

C. Mapping Algorithm From Pixel Pattern to \mathbf{Z}_L

With the prior dataset \mathbf{Z}_{ALL} obtained from the preceding steps, we possess the information needed to compute the performance of arbitrary pixel patterns. The calculation is based on the microwave multiport system formed by all virtual ports.

For a design space with L layers of $M \times N$ (rows \times columns) pixels and with possible vias between layers, any pixel configuration can be represented by an $M \times N \times (2L - 1)$ binary matrix \mathbf{P} . The first $L M \times N$ slices of \mathbf{P} represent presence/absence states of pixels on the L layers, while the following $(L - 1) M \times N$ slices represent presence/absence states of vias between adjacent layers. Specifically, each entry

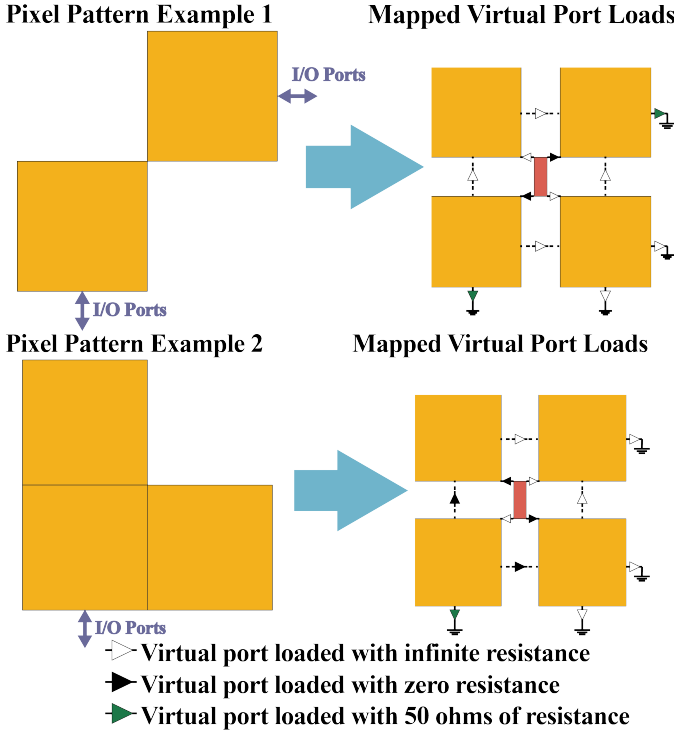


Fig. 4: Two representative examples of how the design space pixel patterns are mapped to the equivalent model in MAPES methodology.

$p_{i,j,l}$, where $1 \leq i \leq M$, $1 \leq j \leq N$, and $1 \leq l \leq 2L - 1$, takes the value 1 or 0: if $1 \leq l \leq L$, $p_{i,j,l} = 1$ indicates a pixel present at position (i, j) on layer l (and 0 indicates absence); if $L + 1 \leq l \leq 2L - 1$, $p_{i,j,l} = 1$ indicates a via present at position (i, j) between layer $(l - L)$ and $(l - L + 1)$ (and 0 indicates absence). Note that a via can exist only between overlapping pixels on adjacent metal layers.

Different connections among pixels can be represented as specific loads (short or open conditions) connected to the multiport system of virtual ports. To facilitate the derivation of the analytical formula in the next subsection, we propose a mapping algorithm that converts any pixel pattern into the corresponding load matrix \mathbf{Z}_L . Assume K I/O ports are chosen among the Q virtual ports; then there are $Q - K$ virtual ports to be assigned loads. Thus $\mathbf{Z}_L = \text{diag}(z_{L,1}, \dots, z_{L,Q-K})$ is a $(Q - K) \times (Q - K)$ diagonal matrix whose diagonal entries represent the loads on the non-I/O virtual ports. An I/O port may be selected from any virtual port. However, for practical convenience we typically place I/O ports on outer pixels, and in this paper we restrict consideration to I/O ports located on outer pixels.

The mapping algorithm is implemented in three processes:

Process 1 (I/O ports): For every virtual port that connects a virtual pixel to ground, if the corresponding original pixel of this virtual pixel is not an I/O pixel, set the load of this virtual port to an open condition (infinite resistance). Remaining I/O virtual ports are not assigned loads because they serve as I/O ports of the final optimized design.

Process 2 (intra-layer and diagonal connections): Consider

Algorithm 1 Pixel Pattern to Load Mapping Algorithm

Input: Pixel pattern \mathbf{P} ($M \times N \times (2L - 1)$ binary matrix)
Output: Load matrix \mathbf{Z}_L ($(Q - K) \times (Q - K)$ diagonal matrix)

- 1: Initialize \mathbf{Z}_L as zero matrix
- 2: **Process 1: Process I/O ports**
- 3: **for** all virtual ports between virtual pixels and ground
- 4: **if** the port is not an I/O port **then**
- 5: Set corresponding load to infinite resistance (open circuit)
- 6: **else**
- 7: Skip mapping (reserved for I/O function)
- 8: **end if**
- 9: **end for**
- 10: **Process 2: Process pixel patterns**
- 11: Initialize all relevant virtual ports loads to zero resistance (short circuit)
- 12: **for** all pixels $p_{i,j,l} \in \mathbf{P}$ (first L layers)
- 13: **if** pixel $p_{i,j,l}$ is in absent state **then**
- 14: Find all virtual ports connected to this absent pixel
- 15: Reset these virtual ports loads from zero to infinite resistance (open circuit)
- 16: **end if**
- 17: **end for**
- 18: **Process 3: Process vias between different layers**
- 19: **for** all vias $p_{i,j,l} \in \mathbf{P}$ (last $L - 1$ layers)
- 20: **if** via $p_{i,j,l}$ is in present state **then**
- 21: Set corresponding virtual ports load to zero resistance (short circuit)
- 22: **else**
- 23: Set corresponding virtual ports load to infinite resistance (open circuit)
- 24: **end if**
- 25: **end for**
- 26: **return** Load matrix \mathbf{Z}_L

all virtual ports that connect virtual pixels to other virtual pixels or to diagonal virtual pixels. Initialize the loads on these ports to short-circuit (zero resistance). Then, for every absent original pixel (as indicated by \mathbf{P}) in the design space, all virtual ports connected to its corresponding virtual pixel will be reset from short (zero resistance) to open (infinite resistance) load. This process converts presence/absence of pixels into the corresponding short/open loads for horizontal, vertical, and diagonal inter-pixel connections.

Process 3 (inter-layer and via ports): For virtual ports that represent potential vias between adjacent layers, set the load to short (zero resistance) if the corresponding via entry in \mathbf{P} is 1, and to open (infinite resistance) if the via entry is 0.

After executing these three processes, the resulting diagonal matrix \mathbf{Z}_L gives the loads corresponding to the specific pixel pattern \mathbf{P} . The proposed mapping algorithm is summarized in Algorithm 1 for clarity. Two representative examples of the

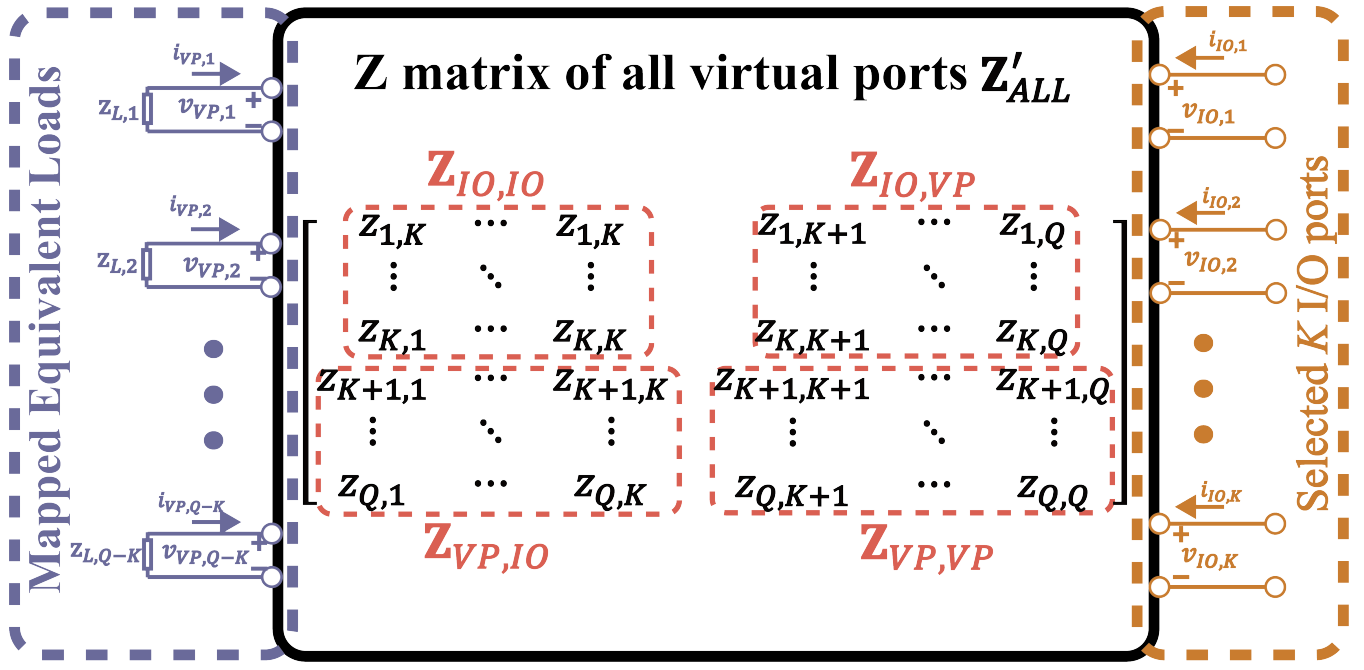


Fig. 5: Model of the multiport network for analytical calculation in the MAPES methodology. The connections between virtual pixels are modelled by the loads specified by Z_L on the left side. The MAPES calculation process uses Z_L with the Z matrix (middle) to determine the Z- or S-parameters of the I/O ports (right).

mapping algorithm are shown in Fig. 4.

D. Analytical Formulas

With the impedance information of all virtual ports, Z_{ALL} , obtained in Subsection II.B and the mapping algorithm that converts an arbitrary pixel pattern to the corresponding load matrix on the virtual ports in Subsection II.C, we have the necessary ingredients to derive analytical expressions for the performance of any pixel pattern at the chosen I/O ports based on microwave multiport theory [31] as shown in Fig. 1(c).

First, we restate the key definitions for better demonstration of the derivation below. Consider a design space with L layers of $M \times N$ (rows \times columns) pixels, with possible vias between adjacent layers. Any pixel configuration can be represented by an $M \times N \times (2L - 1)$ binary matrix \mathbf{P} : the first $L M \times N$ slices indicate presence/absence of pixels on each layer, and the following $(L - 1)$ slices indicate presence/absence of vias between adjacent layers. Select K I/O ports from the Q virtual ports; the remaining $Q - K$ virtual ports are connected to loads and form the non-I/O virtual ports set. The corresponding load matrix of this set is the diagonal matrix $Z_L = \text{diag}(z_{L,1}, \dots, z_{L,Q-K})$, which depends on \mathbf{P} .

For convenience, we reorder the ports of Z_{ALL} so that the selected K I/O ports are located in the first $K \times K$ sub-matrix in Z_{ALL} ; denote this reordered impedance matrix by Z'_{ALL} , which can be partitioned as

$$Z'_{\text{ALL}} = \begin{bmatrix} Z_{IO,IO} & Z_{IO,VP} \\ Z_{VP,IO} & Z_{VP,VP} \end{bmatrix}, \quad (3)$$

where $Z_{IO,IO}$ is the $K \times K$ impedance matrix among the selected K virtual ports for I/O purpose, $Z_{VP,VP}$ is the $(Q - K) \times (Q - K)$ impedance matrix among the unselected virtual

ports, and $Z_{IO,VP}$ and $Z_{VP,IO}$ are the mutual-impedance submatrices between I/O ports and remaining virtual ports. Note that Z'_{ALL} is obtained from Z_{ALL} by a permutation of rows and columns and therefore requires no additional full-wave simulations.

As illustrated in Fig. 5, the virtual ports, the selected I/O ports, and the loads determined from the pixel pattern form a multiport network. Collect the currents at the I/O ports in the vector $\mathbf{I}_{IO} = [i_{IO,1}, \dots, i_{IO,K}]^T$ and the voltages in $\mathbf{V}_{IO} = [v_{IO,1}, \dots, v_{IO,K}]^T$. For the non-I/O (virtual) ports, collect the currents in $\mathbf{I}_{VP} = [i_{VP,1}, \dots, i_{VP,Q-K}]^T$ and the voltages in $\mathbf{V}_{VP} = [v_{VP,1}, \dots, v_{VP,Q-K}]^T$.

By multiport network theory, the port voltages and currents are related by

$$\begin{bmatrix} \mathbf{V}_{IO} \\ \mathbf{V}_{VP} \end{bmatrix} = \begin{bmatrix} Z_{IO,IO} & Z_{IO,VP} \\ Z_{VP,IO} & Z_{VP,VP} \end{bmatrix} \begin{bmatrix} \mathbf{I}_{IO} \\ \mathbf{I}_{VP} \end{bmatrix}. \quad (4)$$

Besides, as in the left side of Fig. 5, for the non-I/O ports connected to loads, the voltage-current relation is also given by

$$\mathbf{V}_{VP} = -Z_L(\mathbf{P})\mathbf{I}_{VP}, \quad (5)$$

where $Z_L(\mathbf{P})$ denotes the diagonal load-impedance matrix mapped from the pixel pattern \mathbf{P} .

Combining (4) and (5) and eliminating the virtual port currents yields

$$\mathbf{V}_{IO} = [Z_{IO,IO} - Z_{IO,VP}(Z_L(\mathbf{P}) + Z_{VP,VP})^{-1}Z_{VP,IO}] \mathbf{I}_{IO}. \quad (6)$$

Equation (6) provides the effective multiport relation at the selected I/O ports for the pixel pattern \mathbf{P} . In other words, for a given pixel pattern \mathbf{P} , the impedance matrix observed

at the I/O ports, denoted $\mathbf{Z}_{\text{MAPES}}(\mathbf{P}) \in \mathbb{C}^{K \times K}$, is obtained analytically as

$$\mathbf{Z}_{\text{MAPES}}(\mathbf{P}) = \mathbf{Z}_{IO,IO} - \mathbf{Z}_{IO,VP}(\mathbf{Z}_L(\mathbf{P}) + \mathbf{Z}_{VP,VP})^{-1}\mathbf{Z}_{VP,IO} \quad (7)$$

Therefore, for any pixel pattern \mathbf{P} we can efficiently compute the corresponding impedance matrix seen at the I/O ports using (7). From $\mathbf{Z}_{\text{MAPES}}(\mathbf{P})$ one can straightforwardly convert to equivalent representations such as scattering (S)-parameters or conductance matrices as required. The submatrices $\mathbf{Z}_{IO,IO}$, $\mathbf{Z}_{IO,VP}$, $\mathbf{Z}_{VP,VP}$, and $\mathbf{Z}_{VP,IO}$ are obtained from the prior one-time full-wave simulations in Fig. 1 and are valid for all pixel patterns \mathbf{P} .

III. MAPES EXAMPLES

By characterizing the entire physical design space using an equivalent model consisting of virtual pixels and virtual ports, the EM behavior over all the design space can be captured by the impedance matrix \mathbf{Z}_{ALL} . For any specific design configuration \mathbf{P} , its performance of interest can then be predicted analytically using (7). Moreover, the proposed MAPES approach is highly general and independent of fabrication technologies or metal stack configurations, making it applicable to both single- and multi-layer RFICs as well as to single- and multi-layer PCBs, with or without metal vias.

To evaluate and demonstrate the efficiency and versatility of the proposed MAPES method, this section presents four representative examples, showcasing how MAPES can be used to calculate the performance of arbitrary pixel patterns efficiently and accurately.

A. CMOS 180 nm Single-Layer Example

To demonstrate the wide applicability of the proposed MAPES methodology to integrated circuit technologies, a single-layer configuration in the CMOS 180 nm RF CMOS process is investigated, as illustrated in Fig. 6. In this example, a thick top-metal layer is utilized as the design layer, while a continuous metal ground plane resides beneath the silicon substrate. The substrate and metallization stack correspond to the CMOS 180 nm process specifications.

As shown in Fig. 6, the pixelated design area is discretized into a 17×17 array, with each pixel measuring $19 \times 19 \mu\text{m}^2$. The total design area is therefore $323 \times 323 \mu\text{m}^2$. The corresponding pixel configuration \mathbf{P} can be represented as a 17×17 binary matrix, where each element indicates the presence or absence of a pixel at the given position. The demonstrated operating frequency range for this example is from 30 to 100 GHz with 71 evenly sampled frequency points.

Following the procedure detailed in Section II.A, the design space is transformed into an array of virtual pixels and diagonal virtual pixels to establish the virtual ports network used in MAPES. As illustrated in Fig. 7, each virtual pixel is slightly smaller than the original pixel, with a physical dimension of $16 \times 16 \mu\text{m}^2$, while diagonal virtual pixels are placed at the corners between adjacent virtual pixels with a dimension of $1 \times 3 \mu\text{m}^2$. Virtual ports are located at the interconnections of virtual pixels and diagonal virtual pixels,

resulting in a total of 1636 virtual ports in this design space. As discussed in Section II.B, 1636 full-wave electromagnetic simulations were carried out using CST MWS to construct the impedance matrix \mathbf{Z}_{ALL} that comprehensively captures all EM coupling information within the defined design space. It should be noted that the conductivity of the top thick metal should be aligned with the process specifications and is usually smaller than the conductivity used in PCB designs.

Once \mathbf{Z}_{ALL} is established, the performance of any arbitrary pixel configuration \mathbf{P} can be predicted analytically using (7) without performing any additional full-wave simulations. To verify the predictive capability and generalization performance of MAPES in this RFIC process, five random pixel configurations were generated, as shown in Fig. 8. For this case, we include eight virtual ports positioned along the edge pixels as the input and output terminals. The upper plots in each subfigure illustrate the randomly generated binary pixel patterns, while the lower plots present both MAPES-predicted and CST-simulated scattering parameters over the 30-100 GHz band.

As depicted in Fig. 8, the predicted S-parameters obtained from MAPES exhibit excellent agreement with those simulated using CST. Since the whole design involves as many as 64 S-parameters, for simplicity and clarity, we only demonstrate four S-parameters in the figures, including S_{11} , S_{24} , S_{28} , and S_{72} . This consistency persists across the entire operating frequency range up to 100 GHz, demonstrating the capability of MAPES to accurately reproduce the electromagnetic response of mmWave structures in RFIC. The results confirm that MAPES can effectively characterize and predict the high-frequency behavior of integrated passive structures with greatly reduced computational cost compared to traditional full-wave electromagnetic solvers.

B. CMOS 65 nm Double-Layer Example

To further validate the accuracy and scalability of the proposed MAPES methodology in integrated circuit technologies, a double-layer design based on the CMOS 65 nm RF process node is investigated, as illustrated in Fig. 9. The structure comprises two metal layers, including the top thick metal and Metal 8 layer, interconnected by an intermediate via layer. A continuous ground plane is located beneath the silicon substrate. This configuration emulates practical multi-metal interconnect structures commonly employed in RF integrated passive components.

As described in Fig. 9, each of the two metal layers contains a design region discretized into a 13×13 pixel array. Each pixel has a physical size of $23 \times 23 \mu\text{m}^2$, corresponding to a total design area of $299 \times 299 \mu\text{m}^2$. The two pixel layers share identical configurations, while the intermediate via layer provides the vertical metal connections between corresponding pixels on the top and bottom layers. The overall pixel configuration \mathbf{P} can therefore be represented as a three-dimensional binary tensor of size $13 \times 13 \times 3$, where the first two dimensions specify the two planar pixel patterns and the third dimension encodes the via layer. The demonstrated frequency range for this example spans from 30 to 100 GHz with 71 evenly sampled frequency points.

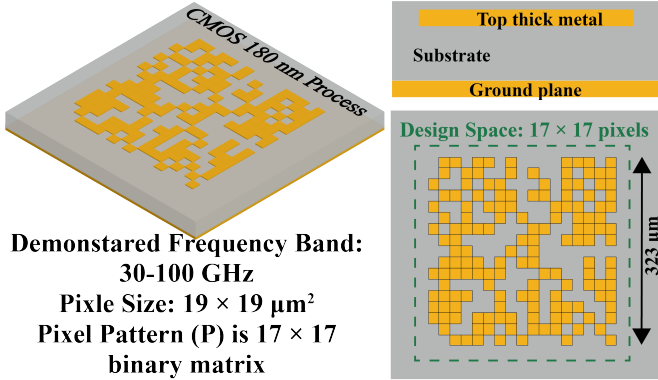


Fig. 6: CMOS 180 nm single-layer pixel design space implemented on the top metal.

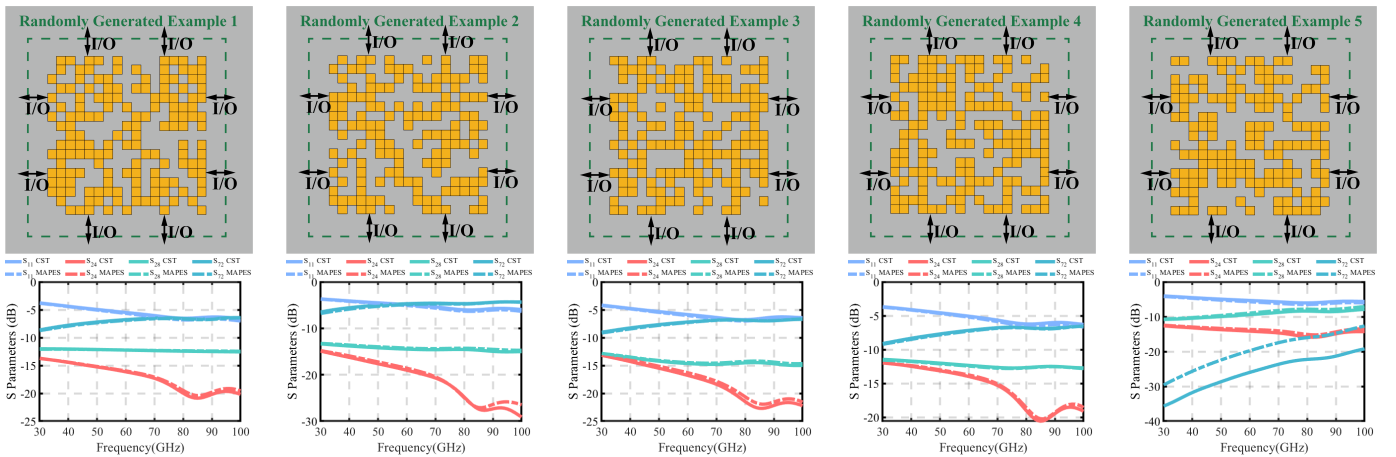


Fig. 8: Five random pixel configurations with S-parameters comparing CST simulations and MAPES predictions.

Following the MAPES preprocessing procedure outlined in Section II.A, each metal layer of the double-layer design space is represented by an equivalent array of virtual pixels and diagonal virtual pixels to introduce virtual ports for electromagnetic coupling characterization. As shown in Fig. 10, each virtual pixel is slightly smaller than the original pixel and has an equivalent size of $20 \times 20 \mu\text{m}^2$, while the diagonal virtual pixels are implemented with dimensions of $1 \times 3 \mu\text{m}^2$. Virtual ports are located around each virtual pixel and also at the via interconnection points. The total number of virtual ports for the double-layer configuration is 2013. Accordingly, 2013 full-wave simulations were conducted in CST Microwave Studio (MWS) to extract the impedance matrix \mathbf{Z}_{ALL} , which comprehensively captures the cross-coupling behavior both within and between the two metal layers through the via network. It should be noted that the conductivities of the top thick metal and Metal 8 layers should be aligned with the process specifications and are usually smaller than the conductivity used in PCB designs.

Once \mathbf{Z}_{ALL} is obtained, the EM performance of any arbitrary dual-layer pixel configuration \mathbf{P} can be analytically predicted using (7) without the need for additional full-wave simulations. It should also be noted that the impedance of vias can be modeled by a practical resistance instead of zero

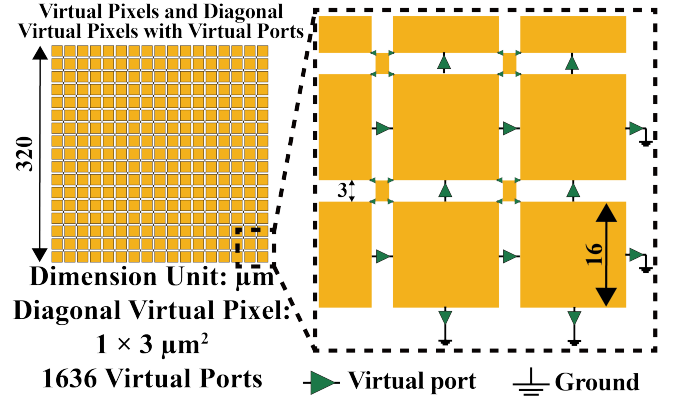


Fig. 7: Virtual pixel and diagonal virtual pixels configurations with virtual ports.

resistance. Five random pixel configurations were generated to evaluate the accuracy and efficiency of MAPES, as illustrated in Fig. 11. In each case, eight virtual ports located along the edges of outer pixels (two in the top thick metal layer and six in the Metal 8 layer) were designated as input and output terminals. The upper subfigures display the pixel patterns on the top thick metal and Metal 8 layers, while the lower subfigures present the corresponding S-parameters computed by MAPES in comparison with CST full-wave simulation results.

As illustrated in Fig. 11, good agreement is observed between the MAPES-predicted and CST-simulated results across the entire 30-100 GHz frequency range. Some minor errors exist when the S-parameters are very low. These well-aligned results validate the capability of MAPES to accurately capture the complex interlayer electromagnetic coupling in deep-submicrometer RFIC processes. Compared with traditional full-wave electromagnetic simulations, the MAPES method achieves significant reductions in computational time while maintaining high fidelity in predicted results. This confirms that MAPES can be effectively applied to model and optimize mmWave multi-layer structures in advanced silicon technologies.

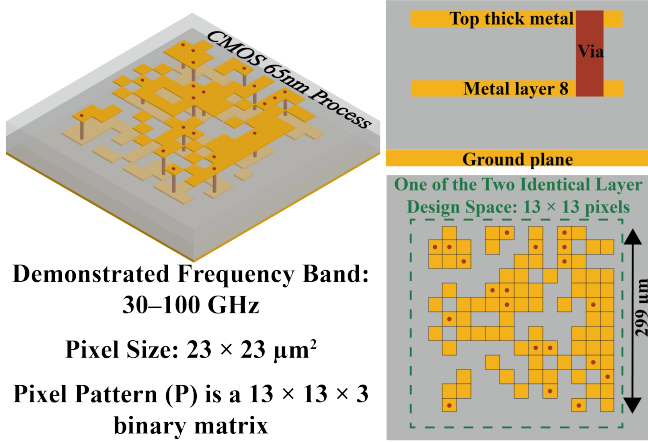


Fig. 9: CMOS 65 nm double-layer pixel design space with via interconnection.

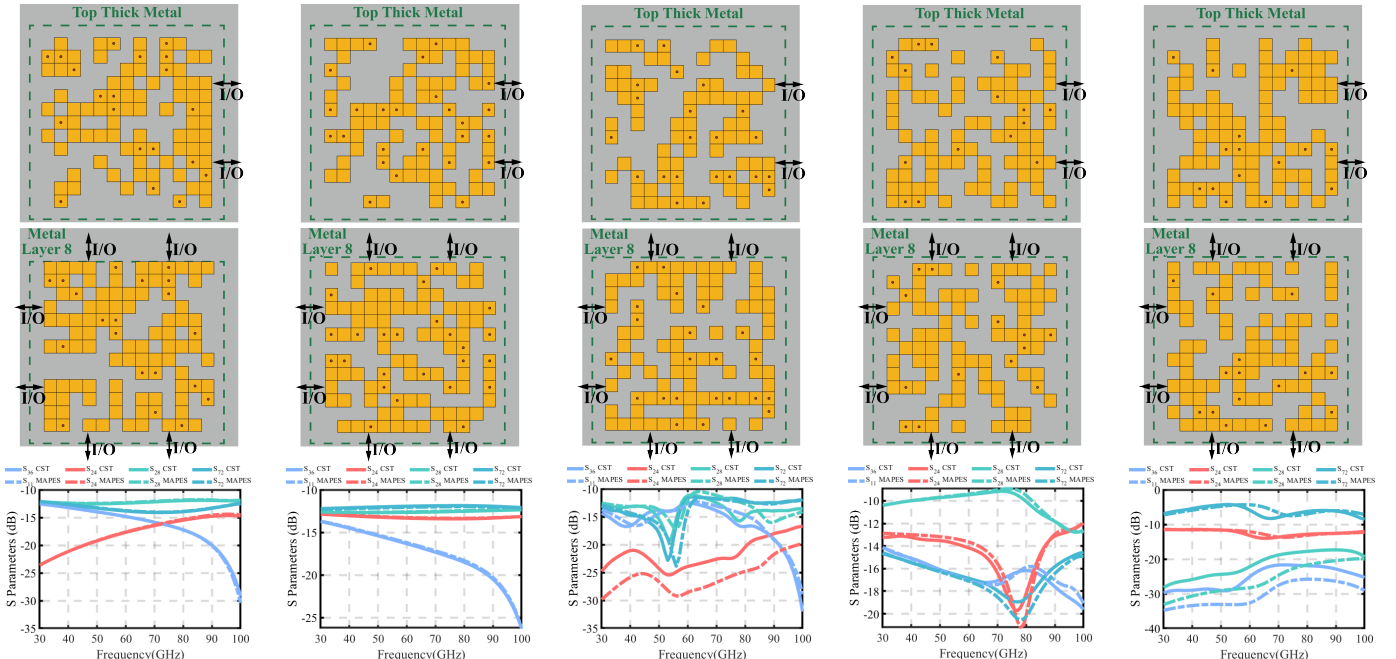


Fig. 10: Virtual pixel and diagonal virtual pixels configuration with virtual ports for both layers.

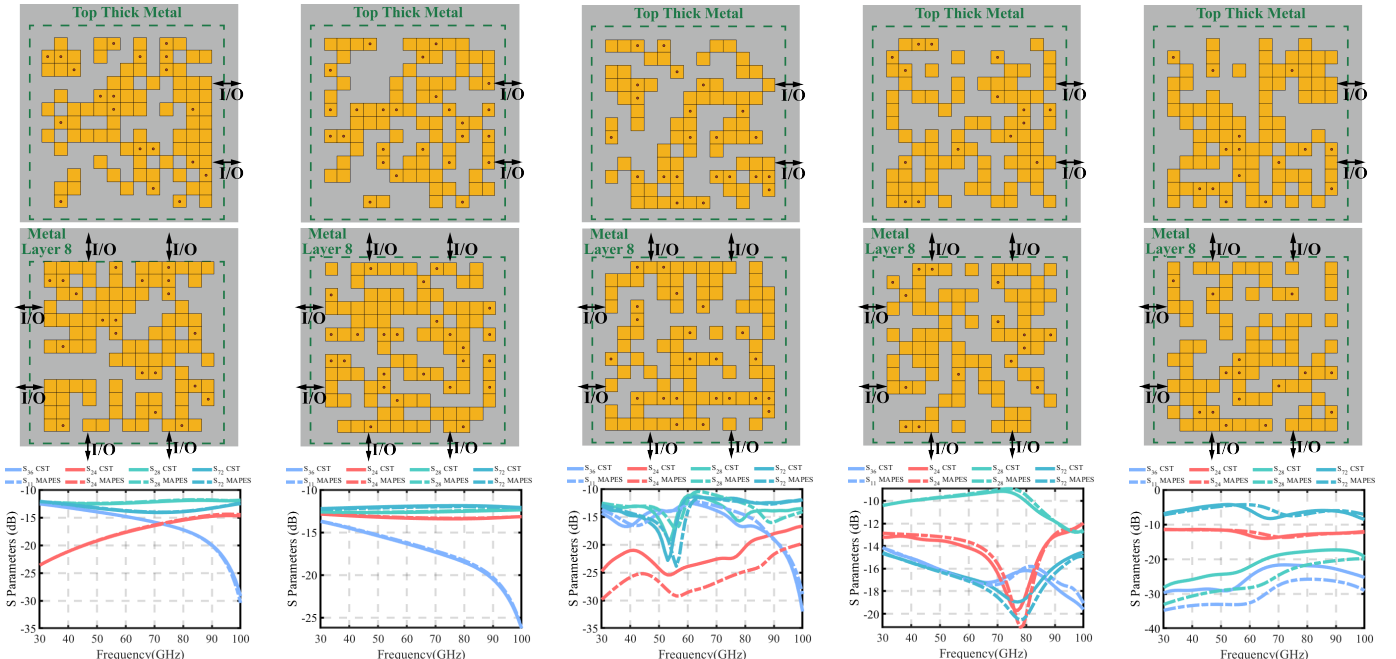


Fig. 11: Five random pixel configurations with S-parameters comparing CST simulations and MAPES predictions.

C. Single-Layer PCB Example

As illustrated in Fig. 12, we consider a single metal layer configuration implemented on a Rogers RO4003C substrate, which has a relative permittivity of $\epsilon_r = 3.55$, a loss tangent of 0.0027, and a substrate thickness of 0.203 mm. A continuous copper ground plane is present on the back side of the substrate. The design area is discretized into a 16×16 pixel array, with each pixel measuring 1.2×1.2 mm 2 . Consequently, the total design area is 19.2×19.2 mm 2 .

Following the procedure described in Section II.A, the design space is represented by an array of virtual pixels and diagonal virtual pixels, as shown in Fig. 13. Each virtual pixel is slightly smaller than its original counterpart, with a physical dimension of 1.0×1.0 mm 2 , allowing insertion of virtual ports between neighboring virtual pixels and diagonal virtual pixels.

The diagonal virtual pixels are located at the intersections of the corners of adjacent virtual pixels. In total, 1444 virtual ports are inserted into the structure according to the procedure detailed in Section II.B.

To obtain the impedance matrix Z_{ALL} that encapsulates the complete EM coupling information of the design space, 1444 full-wave simulations were performed using CST Microwave Studio (MWS). This impedance matrix serves as the prior dataset required for MAPES. The frequency range simulated spans 2-6 GHz with 41 evenly sampled frequency points.

Using the precomputed Z_{ALL} and the analytical expression given by (7), the performance of any arbitrary pixel pattern \mathbf{P} can be efficiently evaluated without additional full-wave simulations. In this example, two virtual ports located on the outer edges of the pixel array are designated as I/O ports.

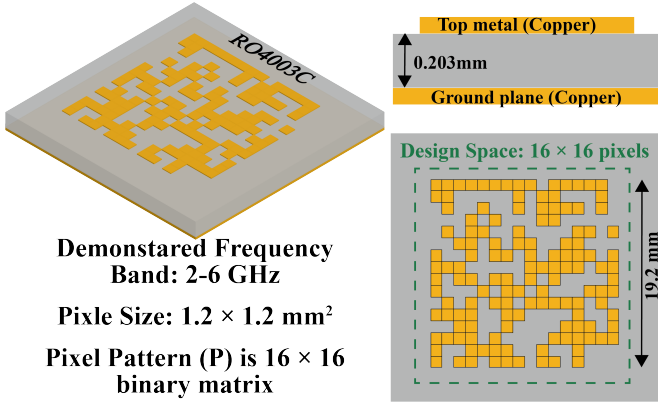


Fig. 12: Single-Layer pixel design space and physical stackup on Rogers RO4003C substrate.

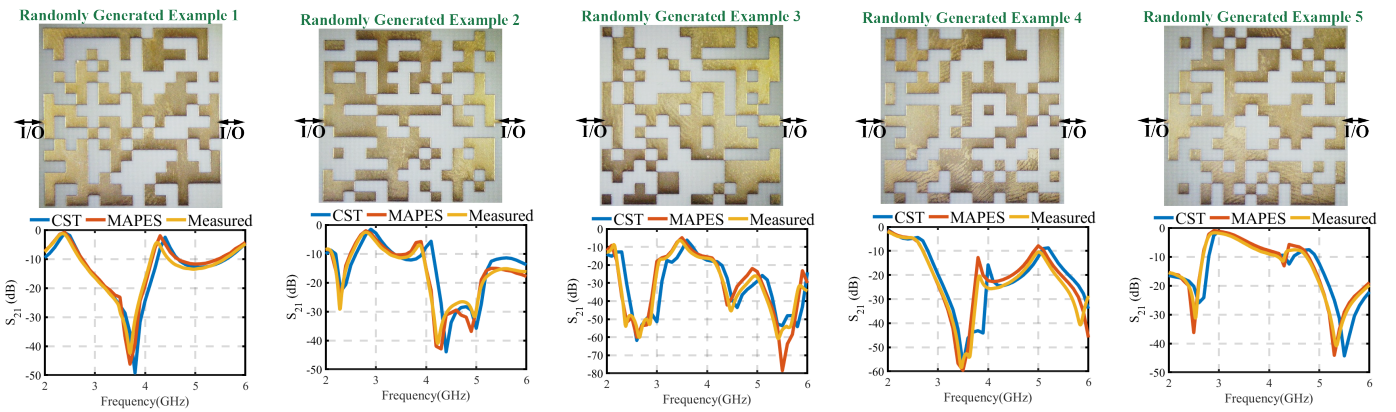


Fig. 14: Five randomly generated pixel patterns with prototypes and S-parameter comparison between CST simulations, MAPES predictions and measured results.

Five random pixel patterns were then generated to verify the accuracy of MAPES predictions.

As shown in Fig. 14, the S-parameter (S_{21}) responses predicted by MAPES (orange curves) are compared with those obtained from full-wave CST simulations (blue curves). The results exhibit very close agreement across the entire frequency band from 2 GHz to 6 GHz. Besides, both of them demonstrate high agreement with the measured results. These examples collectively confirm that MAPES can precisely predict EM performance while achieving significant improvement in computational efficiency compared with conventional full-wave simulation methods.

D. Double-Layer PCB Example

To further verify the flexibility and accuracy of the proposed MAPES method, a double-layer PCB configuration is investigated, as illustrated in Fig. 15. Each metal layer is fabricated on a Rogers RO4003C substrate with the same material properties as in the previous example, that is, a relative permittivity of $\epsilon_r = 3.55$, a loss tangent of 0.0027, and a substrate thickness of 0.203 mm. The structure consists of two identical pixel layers separated by a thin dielectric spacing layer, as shown in the cross-sectional view of Fig. 15. A

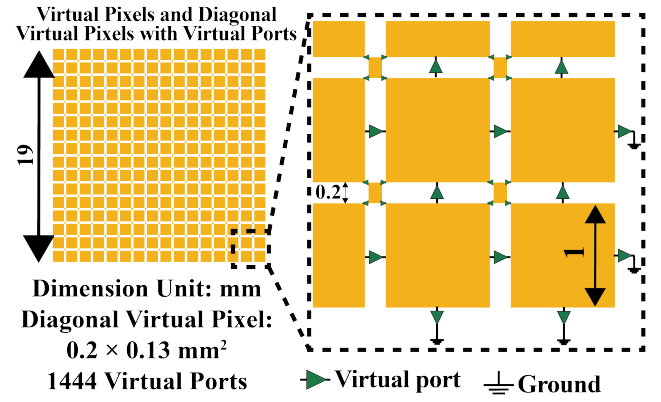


Fig. 13: Virtual pixel and diagonal virtual pixels configurations with virtual ports.

continuous ground plane is located beneath the lower substrate. Vias are also considered between the two pixel layers.

Each metal layer contains a design region discretized into 16×16 pixels, with each pixel having a physical size of $0.61 \times 0.61 \text{ mm}^2$. Consequently, the total design area is $9.76 \times 9.76 \text{ mm}^2$. The two pixel layers share identical configurations, while the intermediate via layer provides interconnection between corresponding pixels on the upper and lower layers. The overall pattern configuration can therefore be represented as a $16 \times 16 \times 3$ binary tensor, where the first and second layers correspond to the metal layers and the third layer represents the via layer. The demonstrated frequency band for this configuration is from 2 to 6 GHz.

Following the procedure described in Section II.A, the entire double-layer design space is transformed into virtual pixels and diagonal virtual pixels, each slightly smaller than the actual pixels. As shown in Fig. 16, the virtual pixel dimension is set to $0.5 \times 0.5 \text{ mm}^2$, and diagonal virtual pixels are inserted at the intersections among adjacent pixels. Virtual ports are assigned both within each layer and along the vias that connect the two layers. The resulting model contains a total of 3144 virtual ports. As detailed in Section II.B, 3144 full-wave simulations were performed using CST MWS to obtain the comprehensive impedance matrix \mathbf{Z}_{ALL} , which serves as the

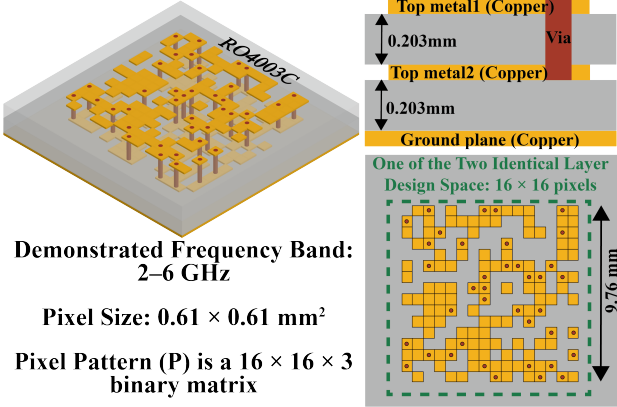


Fig. 15: Double-layer pixel design space with via interconnection.

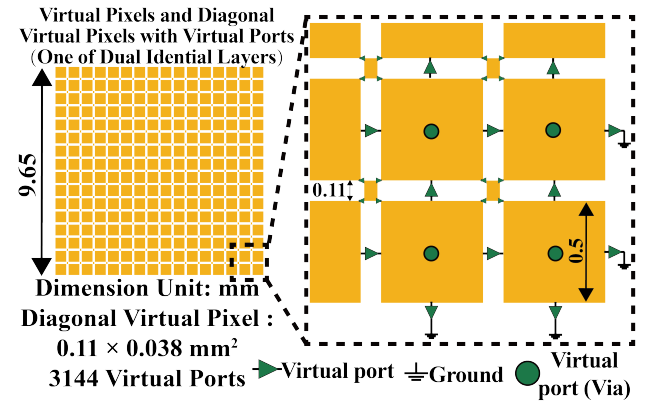


Fig. 16: Virtual pixel and diagonal virtual pixels configuration with virtual ports for both layers.

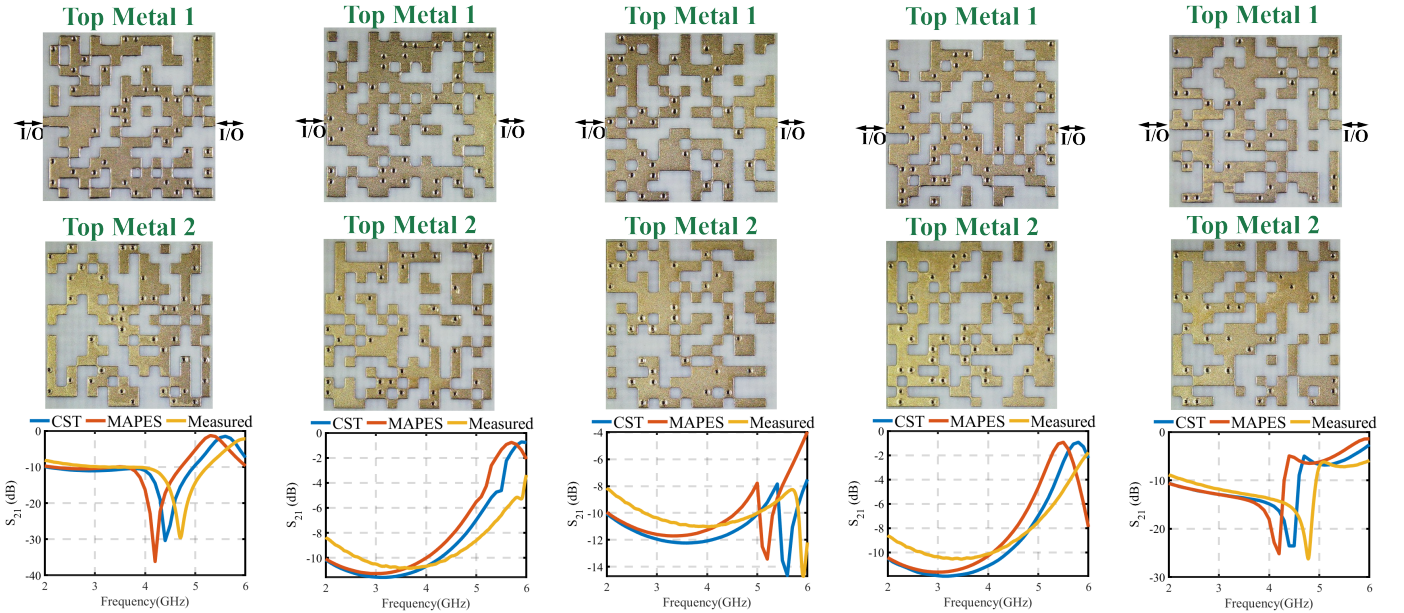


Fig. 17: Five randomly generated dual-layer pixel patterns with prototypes and S-parameter comparison between CST simulations, MAPES predictions and measured results.

TABLE I: Comparison Between MAPES and CST for Different Configurations in Section III

Configuration (Section III)	Design Space	No. of I/O Ports	MAPES Time per Simulation(s)	CST Time per Simulation (s)	Mean Error (E_{mean})	Acceleration Rate
Single-Layer PCB	16 x 16 (pixels)	2	0.391	824	0.2199	2107×
Double-Layer PCB	16 x 16 x 3 (pixels&vias)	2	1.609	991	0.1810	615×
CMOS 180 nm Single-Layer	17 x 17 (pixels)	8	1.028	720	0.0164	700×
CMOS 65 nm Double-Layer	13 x 13 x 3 (pixels&vias)	8	1.4138	2411	0.0275	1705×

Note: All simulations were performed on a workstation equipped with an Intel i7-10700KF CPU and an NVIDIA GTX 3070 GPU. MAPES computations were executed in MATLAB R2024a on the same system. The acceleration rate is defined as the ratio of CST simulation time to MAPES simulation time.

prior dataset for MAPES calculation.

With the established Z_{ALL} and the analytical expression (7), MAPES can rapidly compute the performance of any arbitrary dual-layer pixel pattern \mathbf{P} without requiring further full-wave simulations. Five representative examples of randomly generated dual-layer configurations are presented in Fig. 17. In each case, two virtual ports located at the outer boundary of the

upper layer are selected as excitation and output terminals. The upper and lower pixel patterns corresponding to each random configuration are shown in the upper subfigures, while the calculated performance (S_{21}) versus frequency is plotted in the lower subfigures.

As observed in Fig. 17, the MAPES-calculated results (orange curves) closely match the CST full-wave simulated

results (blue curves) across the entire 2-6 GHz band. The consistency between predicted and simulated responses verifies that MAPES can accurately capture the complex electromagnetic coupling introduced by both inter- and intra-layer interactions. The measured results generally agree with the CST and MAPES predictions. The remaining discrepancies are mainly attributed to the mechanical assembly, where the two PCB layers are fastened with screws rather than fully bonded, leading to imperfect contact between them. This example demonstrates that MAPES is well suited not only for single-layer PCB designs but also for multi-layer structures with interconnecting vias, achieving significant computational efficiency without sacrificing accuracy.

IV. COMPARISON AND DISCUSSION

A. Comparison with Full-Wave Simulations

To quantitatively evaluate the accuracy and computational efficiency of the proposed MAPES framework, its predictions were systematically compared with full-wave electromagnetic simulations performed using CST Microwave Studio for all configurations presented in Section III. Table I summarizes the results of this comparison for each configuration. The comparison metrics include mean magnitude error E_{mean} , computational time, and efficiency improvement in terms of acceleration rate.

The average magnitude error, E_{mean} , between MAPES and CST simulation results is defined as

$$E_{\text{mean}} = \frac{1}{N_{\text{ex}} N_{\text{port}}^2 N_f} \sum_{n=1}^{N_{\text{ex}}} \sum_{m=1}^{N_f} \sum_{i=1}^{N_{\text{port}}} \sum_{j=1}^{N_{\text{port}}} |S_{ij}^{\text{CST}}(f_m, n) - S_{ij}^{\text{MAPES}}(f_m, n)|. \quad (8)$$

where $S_{ij}^{\text{CST}}(f_m, n)$ and $S_{ij}^{\text{MAPES}}(f_m, n)$ represent the ij -th scattering parameter at frequency point f_m for the n -th randomly generated example obtained from CST full-wave simulation and MAPES analytical prediction, respectively. The terms N_{ex} , N_{port} , and N_f correspond to the total number of random examples, the total number of I/O ports, and the number of sampled frequency points, respectively. Thus, E_{mean} quantifies the overall average error across all frequency samples, port combinations, and examples, providing a comprehensive measure of the prediction accuracy of MAPES relative to CST.

The single-layer and double-layer PCB configurations exhibit mean errors of 0.2199 and 0.1810, respectively. These relatively larger deviations are mainly attributed to slight frequency shifts in the resonant response, as observed in Figs. 14 and 17. Nevertheless, the overall amplitude agreement between MAPES and CST remains high across the entire frequency range, indicating that the physical accuracy of MAPES is well maintained. In practical microwave and RF circuit design, these levels of deviation are entirely acceptable, since most design optimization processes can readily account for small frequency offsets and following optimization based on MAPES, such AI or CNN based method, can also take it into considerations.

In contrast, the two integrated-circuit configurations (the CMOS 180 nm single-layer and CMOS 65 nm double-layer designs) demonstrate substantially lower mean errors of 0.0164 and 0.0275, respectively. Additionally, the higher frequency operation and finer metal patterning processes in IC layouts can reduce the impact of boundary discretization errors compared to PCB-scale structures. The great agreement observed in Figs. 8 and 11 further confirms that MAPES can accurately simulate RFIC layouts while having extremely efficiency.

Regarding computational efficiency, MAPES demonstrates dramatic acceleration compared with CST simulations. For example, in the single-layer PCB case, MAPES required only 0.391 s per simulation, whereas CST required approximately 824 s, yielding an acceleration factor exceeding 2100 \times . Similar advantages are observed across the other three configurations, achieving acceleration rates ranging from 615 \times to 1705 \times . These results highlight the fundamental computational advantage of the analytical formulation in (7), which allows the entire EM response to be obtained via a single matrix operation once the prior dataset \mathbf{Z}_{ALL} is established.

Another key observation is that the computational time for CST simulations increases approximately linearly with the number of I/O ports. Each additional port introduces extra excitation requiring a separate full-wave field solution. By contrast, MAPES maintains nearly constant computation time, since the port number only affects the dimension of the submatrix extracted from \mathbf{Z}_{ALL} , and the analytical evaluation in (7) involves only one matrix inversion. Therefore, as the number of I/O ports increases, the relative efficiency advantage of MAPES becomes even more significant. This scalability makes MAPES particularly attractive for complex multiport microwave and RFIC designs, where direct full-wave simulation becomes prohibitively time consuming.

Overall, the results in Table I and corresponding figures clearly demonstrate that MAPES achieves high prediction accuracy across a wide range of configurations while delivering orders-of-magnitude reductions in simulation time. The residual errors, primarily caused by minor frequency shifts in larger PCB structures, remain within acceptable levels. For IC-scale configurations, MAPES attains near-exact agreement with CST results, underscoring its capability to serve as an efficient and accurate alternative to traditional full-wave electromagnetic solvers.

B. Comparison With Other AI-Assisted EM Simulators

Table II summarizes a detailed comparison between the proposed MAPES and several state-of-art AI-assisted EM simulators reported in recent literature. From the results, it is evident that MAPES significantly reduces the required amount of full-wave EM simulations while maintaining high accuracy and generality across all possible structural configurations.

Firstly, for the same or even larger design spaces, MAPES requires only a very small fraction of EM simulations compared with AI-based EM simulators. For instance, in a 16 \times 16 single-layer pixel configuration, MAPES utilizes only 1444 prior datasets, roughly equivalent to 1% of the training data typically required in CNN- or deep-CNN-based EM simulators, which often demand several hundred thousand EM

TABLE II: Comparison Between MAPES and Other AI-Assisted EM Simulators

Configuration	Method	Design Space	Total No. of Possible Designs	Prior/Training Data Size ² (EM Simulation Required)	Relative Percentage ¹ (%)	Potential Over fitting?
Single-Layer PCB (Section.III A)	MAPES	16×16 (pixels)	2^{256}	1444	1.24×10^{-76}	NO
Double-Layer PCB (Section.III B)	MAPES	$16 \times 16 \times 3$ (pixels&vias)	2^{768}	3144	2.02×10^{-230}	NO
Single-Layer CMOS 180 nm (Section.III C)	MAPES	17×17 (pixels)	2^{289}	1636	1.64×10^{-86}	NO
Double-Layer CMOS 65 nm (Section.III D)	MAPES	$13 \times 13 \times 3$ (pixels&vias)	2^{507}	2013	4.80×10^{-152}	NO
Single-Layer PCB [16]	CNN	12×12 (pixels)	2142	500000	8.96×10^{-40}	YES
SiGe 90 nm [5]	Deep-CNN	16×16 (pixels)	2^{256}	340000	2.93×10^{-74}	YES
Single-Layer 90 nm SiGe BiCMOS [13]	CNN	25×25 (pixels)	2^{625}	386000	2.77×10^{-185}	YES
Single-Layer GF 22nm FDX+ [11]	Template-Based CNN	$16 \times 16 \times 2$ (pixels)	2^{512}	52546	3.91×10^{-150}	YES

Note1: The relative percentage represents the ratio between the prior-data/training data size and the entire combinational design space, illustrating the extremely low sampling ratio required by the proposed MAPES framework for effective prior-data simulations.

Note2: The prior-data simulations for MAPES were performed using the CST time-domain solver, which requires exciting the virtual ports sequentially. Consequently, the number of full-wave simulation runs equals the number of virtual ports. In contrast, a frequency-domain solver in CST or HFSS can simulate all virtual ports within a single run to extract the complete multiport matrix, potentially leading to a further reduction in total pre-simulation time for MAPES.

samples for model convergence [16], [5], [13]. This substantial reduction in data requirement directly translates into a dramatic decrease in EM simulation time, making MAPES several orders of magnitude more computationally efficient. For example, generating 1444 prior datasets for MAPES can be completed within a few days using a mid-range workstation, whereas simulating and processing hundreds of thousands of training samples for AI-based networks often requires weeks of high-performance parallel computing resources. Similar conclusions can be drawn for the more complex double-layer PCB and RFIC examples, where MAPES achieves comparable or better accuracy using only a few thousand prior simulations, corresponding to less than $10^{-150}\%$ of the total design space.

All one-time prior-data simulations required by MAPES in Table II were performed using the CST time-domain solver. In this mode, the virtual ports have to be excited sequentially, so the total number of full-wave simulation runs equals the number of virtual ports, as indicated in Note 2 of Table II. If, instead, a frequency-domain solver in CST or HFSS is employed, all virtual ports can be simulated within a single simulation run to extract the complete multiport impedance matrix, which need large RAM memory for large number of virtual ports and can potentially further reduce the one-time pre-simulation cost of MAPES.

Secondly, MAPES provides reliable predictions for all possible design configurations because it is derived directly from first-principles RF multiport network theory rather than from data-driven regression. The impedance matrix \mathbf{Z}_{ALL} fully encapsulates the electromagnetic coupling among all pixels in the defined design space. Any new structure is analytically evaluated through the closed-form formulation in (7), which guarantees physical consistency across all patterns and eliminates statistical uncertainty. In contrast, AI-based EM simulators such as CNNs, deep CNNs, and generative neural networks suffer from inherent generalization and overfitting issues. These models are typically trained on a very limited

subset of the immense combinational design space (e.g., only 10^{-74} to $10^{-185}\%$ coverage, as listed in Table II). As a result, while they perform well on test samples similar to the training distribution, their prediction accuracy may drastically degrade on unseen or irregular pixel configurations. MAPES fundamentally avoids this limitation since every prediction is governed by deterministic analytical relations rather than empirical learning.

It is worth noting that although [11] reports a smaller training dataset relative to a relatively large design space, this efficiency stems from its use of a "template-seeded" data generation strategy specifically designed for transformer geometries. In that approach, the training samples are not randomly drawn from the entire combinational design space but instead constructed from parametric transformer-like templates. As a result, this method may yield high prediction accuracy within transformer design applications but is not generalizable to other device topologies such as filters, couplers, or hybrid microwave structures, where the geometry markedly differs from the predefined template.

On the other hand, while MAPES substantially reduces the reliance on full-wave EM simulations and provides accurate predictions with guaranteed physical consistency, it still involves a computational bottleneck associated with the inversion of a large matrix in (7), which scales with the overall design space dimension. As a result, although MAPES is significantly faster than conventional full-wave solvers, its runtime is still slower than that of purely AI-based EM simulators performing direct regressions through pre-trained neural networks, particularly when both are executed on GPU platforms. As an example, the CNN-based EM simulator in [5] can simulate 4096 different 16×16 pixel designs with only about 0.3 seconds, which is even thousands times faster than MAPES. However, this is also due to the fact that the server (an A100 GPU and 32 AMD EPYC CPU cores) used in [5] is much powerful than one used in this paper.

While MAPES markedly reduces reliance on full-wave EM simulations and delivers reliable predictions, its dominant runtime cost is the matrix inversion in (7). The size of this inversion grows with the number of virtual ports and thus with the overall design-space dimension. Consequently, although MAPES is much faster than conventional full-wave solvers, it can be slower than purely AI-based EM surrogates that evaluate layouts via a single neural-network forward pass on GPUs. For example, the CNN-based simulator in [5] reports evaluating 4096 distinct 16×16 layouts in about 0.3s on a server with an NVIDIA A100 GPU and 32 AMD EPYC CPU cores, orders of magnitude faster than the MAPES implementation used in this work. Part of this gap reflects hardware differences (the server in [5] is substantially more powerful than ours), but it also highlights a fundamental difference of MAPES and AI-assisted EM simulator.

C. Assumptions and Settings for One-Time Pre-Simulation

MAPES fundamentally uses an equivalent model formed by virtual pixels and diagonal virtual pixels, which serve as the physical foundation for the analytical formulation. The underlying assumption governing this modeling approach is illustrated in Fig. 18 using a representative single-layer 3×3 pixel configuration for simplicity.

As shown in Fig. 18, for any arbitrary pixel pattern defined in the original design space (top-left), the mapping algorithm described in Section II.C converts the presence or absence states of the pixels into a corresponding set of load connections among the virtual pixels and diagonal virtual pixels (top-right). These mapped virtual port connections effectively form an equivalent multiport network, on which MAPES performs the analytical computation. In other words, the EM performance predicted by MAPES corresponds to the structure composed of virtual pixels and diagonal virtual pixels with specific interconnections (bottom in Fig. 18) that approximate the original pixel pattern.

The key underlying assumption of MAPES is that the EM response of the mapped virtual pixel structure is equivalent to that of the original pixel pattern. This implies two fundamental premises: (i) the coupling between physically unconnected virtual pixels is negligible, and (ii) the reduction in virtual pixel size (relative to the original pixel) does not significantly distort the EM behavior of the structure. Under these assumptions, MAPES treats the virtual pixel structure as a sufficiently accurate physical alternative of the true pixel-based geometry, enabling the analytical formula in (7) to reliably reproduce the EM response.

However, this assumption introduces an important trade-off in defining the virtual pixel size. If the virtual pixels are chosen too large, approaching the size of the original pixels, the gaps between adjacent virtual pixels become very small, resulting in strong undesired coupling when the corresponding pixels are electrically disconnected. This violates the assumption of negligible mutual coupling and diminishes the accuracy of MAPES predictions. Conversely, if the virtual pixels are defined too small, the physically connected virtual pixels pattern will deviate from the actual pixel pattern too much, leading to

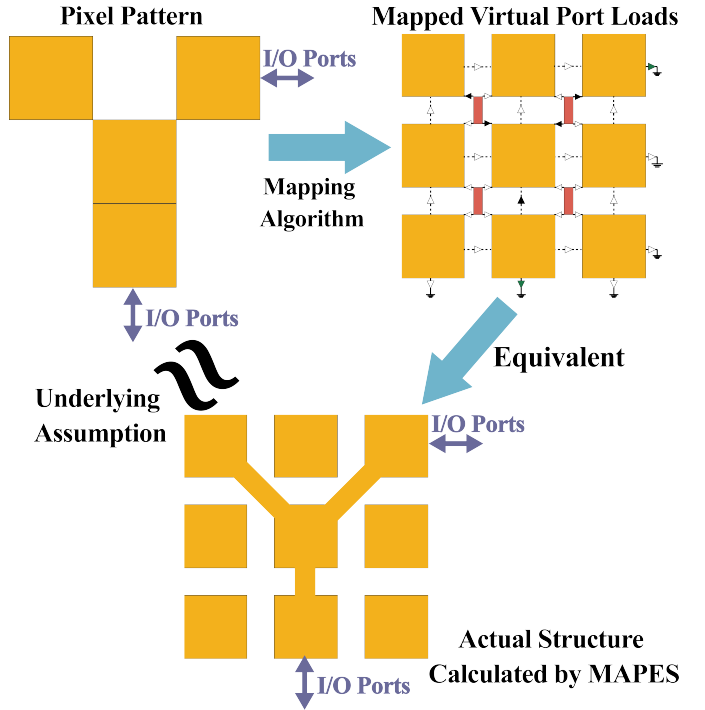


Fig. 18: Illustration of the underlying assumption of MAPES using a single-layer 3×3 pixel example. The original pixel pattern is mapped to an equivalent virtual pixel and diagonal virtual pixel structure whose electromagnetic performance is assumed to be equivalent to the original design.

less accurate results. Both extremes reduce the reliability of MAPES predictions relative to full-wave simulation results.

Therefore, an optimal balance should be maintained between minimizing inter-pixel coupling and preserving realistic pixel pattern. In practice, the suitable virtual pixel size depends on the substrate material, operating frequency, and pixel pitch. As a guideline, for the representative cases demonstrated in Section III including single- and double-layer PCB examples as well as CMOS 180 nm and 65 nm processes, the virtual pixels were set to approximately 85% of the original pixel size. This empirical sizing ensures that the underlying assumptions of MAPES remain valid, allowing accurate analytical prediction of EM performance with negligible deviation from full-wave results.

D. Comparison with MoM-Based Efficient Calculator

A related approach that can also efficiently obtain the electromagnetic performance of arbitrary geometries is the Method of Moments (MoM)-based technique proposed in [28]. In their GA/MoM framework, the primary idea was to precompute the impedance matrix (\mathbf{Z}) of a “mother” structure and then reuse this matrix throughout a GA optimization process by removing the corresponding rows and columns to represent substructures of the mother geometry. This “direct Z-matrix manipulation” enables the electromagnetic response of a large number of structural variations to be evaluated without repeatedly refilling or refactoring the full matrix, thus avoiding the costly full-wave simulation at each iteration. The philosophy behind this

method is therefore conceptually similar to that of MAPES, where the electromagnetic coupling between pixels is captured once and efficiently reused for subsequent performance evaluations.

Nevertheless, when compared with MAPES, several inherent limitations of this MoM-based approach become evident. The method developed in [28] was formulated primarily for planar metallic plates and thin-wire structures excited by voltage or current sources. As such, it does not conveniently include vertical ports, vias, or lumped elements such as switches and tunable loads between pixels. These elements are, however, essential in MW and RFIC designs, where vertical interconnects and vias with non-zero resistance exist. In contrast, MAPES analytically incorporates both horizontal and vertical coupling paths as well as arbitrary lumped loads or active components among the pixels and vias, allowing the comprehensive modeling of I/O ports and realistic non-zero via loads commonly found in various IC processes.

Moreover, the impedance matrix in MAPES can be conveniently obtained directly from standard commercial EM solvers such as CST or HFSS, enabling seamless integration with widely used simulation tools. In the MoM-based approach, however, the impedance matrix of meshes is an intermediate data that is generally inaccessible in commercial software and requires specialized coding or in-house implementations to compute. Consequently, while both methods rely on the idea of reusing a precomputed impedance representation, MAPES provides broader modeling flexibility, easier accessibility, and superior computational scalability.

Another limitation lies in the mesh resolution and computational scalability of the MoM framework. Each substructure is represented using sets of wire and surface basis functions, such as the Rao-Wilton-Glisson (RWG) basis defined on triangular mesh elements [29]. To accurately model pixel-based geometries, the mesh size in MoM must be much finer than the pixel dimensions to capture detailed current distributions. This fine meshing significantly increases both the number of unknowns and the size of the impedance matrix, resulting in large memory and computation demands. As the design space grows, especially when multiple layers are considered, the dense matrix operations required by MoM become computationally prohibitive. In contrast, MAPES only places ports at essential electrical locations, leading to a much more compact mathematical representation and substantially reduced matrix size, thereby achieving higher computational efficiency for large-scale pixel arrays.

Recently, the precomputed numerical Green-function (PNGF) framework in [30] extended the MoM-style “efficient calculator” philosophy to general full-wave environments. In PNGF, the static environment is absorbed into a numerical Green matrix \mathbf{G} , obtained once using either custom FDTD/FDFD solvers or commercial tools such as HFSS/CST, and candidate layouts are then evaluated by solving reduced linear systems for equivalent polarization currents confined to the optimization region. Compared to the original MoM efficient calculator, PNGF therefore inherits two important advantages that are also characteristic of MAPES: (i) the underlying operator (\mathbf{G}) can be generated directly by commercial

full-wave solvers without exposing internal MoM matrices, and (ii) fully three-dimensional structures with vertical features, stacked substrates and waveguiding elements can be treated in a unified manner. From the viewpoint of pixel-based RFIC/PCB layout exploration, however, PNGF operates on a system matrix whose dimension is the number of field unknowns in the optimization region, N_{opt} , i.e., the number of Yee-cell edges or FEM/BEM basis functions. In practice N_{opt} typically scales as $N_{\text{opt}} \approx N_{\text{pixel}} \times N_{\text{cell/pixel}}$, and accurate discretizations often require tens of mesh cells per pixel (e.g., 20–30), so the linear-algebra cost and memory footprint remain substantially larger than those of MAPES, whose core matrices have size $(4\text{--}6) \times N_{\text{pixel}}$ and are independent of mesh density. Furthermore, the Woodbury low-rank update strategy [30], [32] used in PNGF to accelerate direct-binary-search optimization when only one or a few tiles change per iteration is equally applicable to MAPES: when a design step modifies only a small subset of pixel/via loads in \mathbf{Z}_L , the effective I/O matrix in (7) can, in principle, be updated via low-rank corrections rather than recomputing a full inverse, offering an additional route to further speed up large-scale MAPES-based inverse design.

E. Potential Applications of MAPES

MAPES exhibits strong potential for integration into future AI-assisted MW circuit and RFIC design frameworks. The potential applications include but not limited to:

- 1) *Replacement of AI-Based EM Simulators:* MAPES can serve as an efficient and physically rigorous substitute for conventional AI-based EM simulators. Since it is derived from the RF multiport network theory, MAPES can directly evaluate the electromagnetic behavior of arbitrary pixel-based or multiport structures without depending on data-driven approximations. Accordingly, inverse-design methodologies, such as heuristic optimization [5], simulated annealing, or emerging generative AI-based tools like autoencoders, tandem neural networks [16], and diffusion models [12], can be integrated with MAPES to achieve rapid structural synthesis.
- 2) *Generation of Training Datasets:* MAPES can be effectively utilized as a high-speed data generator for constructing large-scale training datasets required by AI-assisted EM simulators. Once a comparatively small prior dataset (about only 1% of that required by an AI-based EM simulator) is generated to establish the global impedance matrix \mathbf{Z}_{ALL} , MAPES can thereafter generate EM response datasets 500–1000 times faster than full-wave solvers, as demonstrated in Table I. This accelerated dataset generation drastically reduces computational costs associated with training data preparation, thereby enabling CNN/NN-based EM models to efficiently explore much larger design spaces and complex multi-layer structures with vias, domains that would otherwise be infeasible using conventional full-wave EM tools.
- 3) *Enabling multi-fidelity inverse design:* One inherent limitation of purely AI-assisted EM simulators is that,

although they can provide very fast and reasonably accurate predictions over the whole design space, they often struggle to capture fine spectral details, sharp resonances, or strong coupling effects, especially for layouts that deviate from the training distribution. As a result, inverse design workflows that rely solely on such low-fidelity surrogates may converge to layouts whose performance degrades noticeably when re-evaluated with a high-fidelity full-wave solver. Owing to its stable and yet highly efficient analytical nature, MAPES can act as an additional fidelity level within a multi-fidelity optimization or inverse-design framework [33], [34]. For example, a fast CNN-based surrogate can be used for global exploration and candidate generation, while MAPES is employed in the refinement stage to re-rank promising designs, correct coarse predictions, and provide more reliable responses before a final, sparse validation with CST/HFSS. In this way, MAPES not only serves as a stand-alone high-fidelity simulator, but also functions as a robust physical anchor that enhances the reliability, robustness, and convergence of multi-fidelity inverse-design pipelines.

- 4) *Enabling reinforcement learning-based layout optimization:* MAPES can also serve as a fast, physics-based environment for reinforcement learning (RL) agents in RF passive circuit design [35], [36]. After the one-time construction of the global impedance matrix using a limited set of full-wave simulations, MAPES can rapidly evaluate arbitrary pixel/via patterns within the design space by computing their S-parameters and returning a scalar reward that reflects how well each layout meets given specifications (e.g., insertion loss, return loss, isolation, bandwidth, and area). An RL agent then treats the pixel/via occupancy matrix as its state, takes actions that modify the layout (such as toggling pixels or vias), and receives MAPES-based rewards to iteratively learn an effective design policy over many episodes. This integration enables data-efficient, closed-loop AI-driven layout optimization that remains grounded in accurate electromagnetic physics while avoiding the prohibitive cost of calling a full-wave solver at every RL step.
- 5) *Development of AI-Accelerated MAPES Models:* Although MAPES achieves substantial speed-ups compared to full-wave EM simulations, its computation time remains dominated by the matrix inversion process in (7). To mitigate this limitation, future research could explore the integration of AI-driven or high-performance numerical schemes specifically designed for fast matrix inversion [37], [38], [39]. By leveraging GPU-based computation or neural-network-assisted inversion algorithms, MAPES could achieve prediction speeds comparable to those of purely data-driven simulators, while preserving its underlying physical rigor. Moreover, since MAPES inherently adheres to electromagnetic theory, any AI models built atop MAPES outputs will exhibit improved generalization with reduced overfitting and bias. The required prior and training datasets for such hybrid AI-MAPES models would also be substantially

smaller than those for conventional deep-learning-based EM simulation approaches.

V. CONCLUSION

This paper has proposed and validated MAPES, an analytical, physics-driven method for fast and accurate electromagnetic simulation of arbitrary pixel-based MW circuits and RFICs. Through the introduction of diagonal virtual pixels and systematically placed virtual ports, MAPES captures the complete electromagnetic coupling environment across horizontal, vertical, and diagonal directions within a compact multiport impedance matrix. This matrix, obtained through only a limited number of full-wave simulations, encodes all the physical information of the design space and allows analytical prediction of any structural configuration using a unified closed-form formulation derived from multiport network theory.

Comprehensive results across single- and multi-layer PCB and CMOS processes validate the exceptional accuracy and scalability of MAPES. Compared to full-wave CST simulations, MAPES delivers 600-2000 \times acceleration while maintaining excellent correlation of S-parameters. Unlike data-driven AI-based EM simulators, MAPES inherently avoids overfitting, generalizes to all possible geometries, and seamlessly supports models with vias and multi-layer interconnections.

Beyond serving as a stand-alone EM simulator, MAPES can act as a rapid dataset generator for AI training or as a physical backbone for hybrid physics-informed neural network. Future research may further enhance MAPES by incorporating GPU-accelerated or AI-assisted matrix inversion techniques to further boost its simulation speed. Overall, MAPES establishes an efficient, physically interpretable, and fabrication-compatible solution for next-generation AI-assisted electromagnetic modeling and RFIC/microwave circuit design.

REFERENCES

- [1] L. Chettri and R. Bera, "A comprehensive survey on internet of things (iot) toward 5g wireless systems," *IEEE Internet of Things Journal*, vol. 7, no. 1, pp. 16–32, 2020.
- [2] M. Shafi, A. F. Molisch, P. J. Smith, T. Haustein, P. Zhu, P. De Silva, F. Tufvesson, A. Benjebbour, and G. Wunder, "5g: A tutorial overview of standards, trials, challenges, deployment, and practice," *IEEE Journal on Selected Areas in Communications*, vol. 35, no. 6, pp. 1201–1221, 2017.
- [3] W. Saad, M. Bennis, and M. Chen, "A vision of 6g wireless systems: Applications, trends, technologies, and open research problems," *IEEE Network*, vol. 34, no. 3, pp. 134–142, 2020.
- [4] C.-X. Wang, X. You, X. Gao, X. Zhu, Z. Li, C. Zhang, H. Wang, Y. Huang, Y. Chen, H. Haas, J. S. Thompson, E. G. Larsson, M. D. Renzo, W. Tong, P. Zhu, X. Shen, H. V. Poor, and L. Hanzo, "On the road to 6g: Visions, requirements, key technologies, and testbeds," *IEEE Communications Surveys & Tutorials*, vol. 25, no. 2, pp. 905–974, 2023.
- [5] E. A. Karahan, Z. Liu, and K. Sengupta, "Deep-learning-based inverse-designed millimeter-wave passives and power amplifiers," *IEEE Journal of Solid-State Circuits*, vol. 58, no. 11, pp. 3074–3088, 2023.
- [6] K. Chen and D. Peroulis, "Design of highly efficient broadband class-e power amplifier using synthesized low-pass matching networks," *IEEE Transactions on Microwave Theory and Techniques*, vol. 59, no. 12, pp. 3162–3173, 2011.
- [7] J.-W. Lin, C. Chen, and Y.-T. Cheng, "A robust high-q micromachined rf inductor for rfic applications," *IEEE Transactions on Electron Devices*, vol. 52, no. 7, pp. 1489–1496, 2005.

- [8] E. Wilkinson, "An n-way hybrid power divider," *IRE Transactions on Microwave Theory and Techniques*, vol. 8, no. 1, pp. 116–118, 1960.
- [9] C. Yue and S. Wong, "On-chip spiral inductors with patterned ground shields for si-based rf ics," *IEEE Journal of Solid-State Circuits*, vol. 33, no. 5, pp. 743–752, 1998.
- [10] C. Chu, E. Liu, Y. Liu, B. Lin, M. Eleraky, B. Abdelaziz, M. Ghorbanpoor, T.-Y. Huang, A. Wang, and H. Wang, "Deep learning-assisted rfic design with dual-metal-layer passive matching networks: A 15–22 ghz cmos pa for 6g in 22nm fdx+," in *2025 16th German Microwave Conference (GeMiC)*, 2025, pp. 76–79.
- [11] C. Chu, J. Xu, Y. Liu, J. Zeng, A. Wang, T. Torii, S. Shinjo, K. Yamamoto, and H. Wang, "Ai-assisted template-seeded pixelated design for multi-metal-layer high-coupling em structures: A ku-band 6g fr3 pa in 22nm fdx+," in *2025 IEEE/MTT-S International Microwave Symposium - IMS 2025*, 2025, pp. 922–925.
- [12] Y. Guo, E. A. Karahan, Z. Li, Z. Shao, Z. Zhang, M. Wang, and K. Sengupta, "Dall-em: Generative ai with diffusion models for new design space discovery and target-to-electromagnetic structure synthesis," in *2025 IEEE/MTT-S International Microwave Symposium - IMS 2025*, 2025, pp. 926–929.
- [13] E. A. Karahan, Z. Liu, and K. Sengupta, "Ims deep learning enabled generalized synthesis of multi-port electromagnetic structures and circuits for mmwave power amplifiers," in *2024 IEEE/MTT-S International Microwave Symposium - IMS 2024*, 2024, pp. 184–187.
- [14] E. A. Karahan, Z. Liu, A. Gupta, Z. Shao, J. Zhou, U. Khankhoe, and K. Sengupta, "Deep-learning enabled generalized inverse design of multi-port radio-frequency and sub-terahertz passives and integrated circuits," *Nature communications*, vol. 15, no. 1, p. 10734, 2024.
- [15] V. Chenna and H. Hashemi, "Algorithmic design and optimization of on-chip multilayered pixelated passive networks," *IEEE Transactions on Microwave Theory and Techniques*, pp. 1–11, 2025.
- [16] A. Gupta, E. A. Karahan, C. Bhat, K. Sengupta, and U. K. Khankhoe, "Tandem neural network based design of multiband antennas," *IEEE Transactions on Antennas and Propagation*, vol. 71, no. 8, pp. 6308–6317, 2023.
- [17] I. Goodfellow, Y. Bengio, A. Courville, and Y. Bengio, *Deep learning*. MIT press Cambridge, 2016, vol. 1, no. 2.
- [18] N. Srivastava, G. Hinton, A. Krizhevsky, I. Sutskever, and R. Salakhutdinov, "Dropout: a simple way to prevent neural networks from overfitting," *The journal of machine learning research*, vol. 15, no. 1, pp. 1929–1958, 2014.
- [19] J. Araque and G. Vecchi, "A compact antenna reconfigurable in the band 1.7ghz - 2.7ghz," in *2006 IEEE Antennas and Propagation Society International Symposium*, 2006, pp. 2333–2336.
- [20] S. Song and R. D. Murch, "An efficient approach for optimizing frequency reconfigurable pixel antennas using genetic algorithms," *IEEE Transactions on Antennas and Propagation*, vol. 62, no. 2, pp. 609–620, 2014.
- [21] S. Shen, C.-Y. Chiu, and R. D. Murch, "Multiport pixel rectenna for ambient rf energy harvesting," *IEEE Transactions on Antennas and Propagation*, vol. 66, no. 2, pp. 644–656, 2018.
- [22] Y. Zhang, S. Tang, J. Rao, C.-Y. Chiu, X. Chen, and R. Murch, "A dual-port dual-beam pattern-reconfigurable antenna with independent 2-d beam-scanning," *IEEE Transactions on Antennas and Propagation*, vol. 72, no. 10, pp. 7628–7643, 2024.
- [23] J. Rao, Z. Ming, J. Zhang, C.-Y. Chiu, and R. Murch, "Cost-effective enhancement of rf switch performance utilizing novel coupling structures," *IEEE Transactions on Microwave Theory and Techniques*, pp. 1–17, 2025.
- [24] J. Rao, Z. Ming, J. Zhang, Z. Li, C.-Y. Chiu, and R. Murch, "A compact shared-aperture antenna with 2-transmit and 2-receive highly-isolated ports for full-duplex mimo systems," *IEEE Open Journal of Antennas and Propagation*, vol. 6, no. 2, pp. 422–432, 2025.
- [25] J. Rao, Y. Zhang, S. Tang, Z. Li, Z. Ming, J. Zhang, C.-Y. Chiu, and R. Murch, "A shared-aperture dual-band sub-6 ghz and mmwave reconfigurable intelligent surface with independent operation," *IEEE Transactions on Microwave Theory and Techniques*, vol. 73, no. 7, pp. 4116–4132, 2025.
- [26] J. Zhang, J. Rao, Z. Li, Z. Ming, C.-Y. Chiu, K.-K. Wong, K.-F. Tong, and R. Murch, "A novel pixel-based reconfigurable antenna applied in fluid antenna systems with high switching speed," *IEEE Open Journal of Antennas and Propagation*, vol. 6, no. 1, pp. 212–228, 2025.
- [27] L. Jing, M. Li, and R. Murch, "Compact pattern reconfigurable pixel antenna with diagonal pixel connections," *IEEE Transactions on Antennas and Propagation*, vol. 70, no. 10, pp. 8951–8961, 2022.
- [28] J. Johnson and Y. Rahmat-Samii, "Genetic algorithms and method of moments (ga/mom) for the design of integrated antennas," *IEEE Transactions on Antennas and Propagation*, vol. 47, no. 10, pp. 1606–1614, 1999.
- [29] S. Makarov, "Mom antenna simulations, with matlab: Rwg basis functions," *IEEE Antennas and Propagation Magazine*, vol. 43, no. 5, pp. 100–107, 2002.
- [30] J.-H. Sun, M. Elsawaf, Y. Zheng, H.-C. Lin, C. W. Hsu, and C. Sideris, "Ultrafast inverse design of electromagnetic devices," *arXiv preprint arXiv:2501.18054*, 2025.
- [31] D. M. Pozar, *Microwave engineering: theory and techniques*. John wiley & sons, 2021.
- [32] S. S. Bayin, *Mathematical methods in science and engineering*. John Wiley & Sons, 2018.
- [33] M. G. Fernández-Godino, "Review of multi-fidelity models," *arXiv preprint arXiv:1609.07196*, 2016.
- [34] H. S. Kim, M. Koc, and J. Ni, "A hybrid multi-fidelity approach to the optimal design of warm forming processes using a knowledge-based artificial neural network," *International Journal of Machine Tools and Manufacture*, vol. 47, no. 2, pp. 211–222, 2007.
- [35] A. Mirhoseini, A. Goldie, M. Yazgan, J. W. Jiang, E. Songhori, S. Wang, Y.-J. Lee, E. Johnson, O. Pathak, A. Nova *et al.*, "A graph placement methodology for fast chip design," *Nature*, vol. 594, no. 7862, pp. 207–212, 2021.
- [36] R. S. Sutton, A. G. Barto *et al.*, *Reinforcement learning: An introduction*. MIT press Cambridge, 1998, vol. 1, no. 1.
- [37] G. Sharma, A. Agarwala, and B. Bhattacharya, "A fast parallel gauss jordan algorithm for matrix inversion using cuda," *Computers & Structures*, vol. 128, pp. 31–37, 2013.
- [38] Y. Zhang, S. Li, J. Weng, and B. Liao, "Gnn model for time-varying matrix inversion with robust finite-time convergence," *IEEE Transactions on Neural Networks and Learning Systems*, vol. 35, no. 1, pp. 559–569, 2022.
- [39] J. Jin, J. Zhu, L. Zhao, L. Chen, L. Chen, and J. Gong, "A robust predefined-time convergence zeroing neural network for dynamic matrix inversion," *IEEE Transactions on Cybernetics*, vol. 53, no. 6, pp. 3887–3900, 2023.